

Scicchitano, M. R., Lafay, R., Valley, J. W., Kita, N. T., Nachlas, W. O. (2022): Protracted hydrothermal alteration recorded at the microscale in the Chenaillet ophicarbonates (Western Alps): Insights from in situ $\delta^{18}\text{O}$ thermometry in serpentine, carbonate and magnetite. - *Geochimica et Cosmochimica Acta*, 318, 144-164.

<https://doi.org/10.1016/j.gca.2021.11.025>

1 Protracted hydrothermal alteration recorded at the microscale in
2 the Chenaillet ophicarbonates (Western Alps): Insights from *in*
3 *situ* $\delta^{18}\text{O}$ thermometry in serpentine, carbonate and magnetite

4

5 Maria Rosa Scicchitano^{a, b, *}, Romain Lafay^c, John W. Valley^b, Noriko T. Kita^b,
6 William O. Nachlas^b

7

8 ^a Deutsches GeoForschungsZentrum GFZ, D14473 Potsdam, Germany (maria.rosa.scicchitano@gfz-
9 potsdam.de)

10 ^b Department of Geoscience, University of Wisconsin, Madison 53706, WI, USA
11 (valley@geology.wisc.edu, noriko@geology.wisc.edu, nachlas@wisc.edu)

12 ^c Géosciences Montpellier, Université Montpellier-II, 34095 Montpellier, France
13 (romain.lafay@yahoo.fr)

14

15 * Corresponding author. E-mail: maria.rosa.scicchitano@gfz-potsdam.de

16

17 Keywords: ophicarbonates, Alps, oxygen isotopes, geothermometry, SIMS

18

19

20

21

22

23

24

25

26

27 **Abstract**

28

29 The study of serpentinites and ophicarbonates from ophiolitic terrains provides a
30 three-dimensional perspective on the hydration and carbonation processes affecting
31 modern oceanic lithosphere. The Chenaillet ophiolite (western Alps) is interpreted as
32 a fragment of an oceanic core complex that resembles a modern slow spreading
33 center, and it was weakly affected by Alpine metamorphism. Ophicarbonates from the
34 Chenaillet ophiolite were targeted in this study for *in situ* analysis by Secondary Ion
35 Mass Spectrometry (SIMS) of oxygen and carbon isotopes in serpentine, calcite,
36 dolomite and magnetite. The high spatial resolution of SIMS allowed us to target
37 different serpentine, carbonate and magnetite generations intergrown at scales ≤ 50
38 μm , and reveal systematic zoning in $\delta^{18}\text{O}$ with a range of 5.8‰ in serpentine (from
39 3.0 to 8.8‰, V-SMOW), 21.2‰ in carbonate (9.4 to 30.6‰), and 5.6‰ in magnetite
40 (−5.0 to −10.6‰). Coupled analysis of oxygen isotopes in seven different touching-
41 pairs of co-crystallized serpentine+carbonate and serpentine+magnetite provides
42 independent constraints on both the temperatures and $\delta^{18}\text{O}_{(\text{water})}$ values during
43 serpentinization and carbonation responsible for the formation of the Chenaillet
44 ophicarbonates. The new stable isotope data and thermometric estimates can be
45 directly linked to textural and petrographic observations. These new results identify at
46 least four different stages of hydrothermal alteration in the Chenaillet ophicarbonates:
47 (1) peridotite hydration during seafloor exhumation at temperatures down to 200-130
48 °C and water $\delta^{18}\text{O}$ values varying from 5 to 2‰, as documented by
49 serpentine+magnetite in mesh textures; (2) carbonation during exhumation near the
50 seafloor at temperatures as low as 10 °C assuming water $\delta^{18}\text{O}$ values of −1‰, as
51 documented by the highest oxygen isotope ratios in texturally older calcite; (3)

52 serpentinization and carbonation at temperatures up to 240 °C and water $\delta^{18}\text{O}$ values
53 of 2-3‰, as documented by serpentine+magnetite in veins crosscutting mesh textures
54 ($T = 192 \pm 66$ °C, $\delta^{18}\text{O}_{(\text{water})} = 2 \pm 1$ ‰, 2 standard deviation), serpentine+magnetite ($T =$
55 182 ± 32 °C, $\delta^{18}\text{O}_{(\text{water})} = 2 \pm 1$ ‰) and serpentine+dolomite ($T = 243 \pm 79$ °C, $\delta^{18}\text{O}_{(\text{water})} =$
56 3 ± 2 ‰) in recrystallized hourglass domains within serpentinite clasts,
57 serpentine+dolomite ($T = 229 \pm 50$ °C, $\delta^{18}\text{O}_{(\text{water})} = 3 \pm 1$ ‰) and serpentine+calcite ($T =$
58 208 ± 40 °C, $\delta^{18}\text{O}_{(\text{water})} = 2 \pm 1$ ‰) within the fine-grained calcite matrix surrounding
59 serpentinite clasts; (4) late stage carbonation at temperatures down to 70-40 °C
60 assuming water $\delta^{18}\text{O}$ values of 3 to -1‰, as documented by the highest oxygen
61 isotope ratios in a large calcite vein crosscutting both serpentinite clasts and fine-
62 grained carbonate matrix. We suggest that the textural and isotopic observations are
63 consistent with a protracted serpentinization and carbonation of the lithospheric
64 mantle that started during progressive exhumation to the seafloor and continued due
65 to interaction with hot and isotopically shifted seawater, which circulated at depth in
66 the oceanic crust and was then discharged near the seafloor, similar to modern mid-
67 ocean ridge venting systems.

68

69

70

71

72

73

74

75

76

1. INTRODUCTION

77

78

79 Serpentinization and carbonation of ultramafic rocks occur over a wide range of
80 environments and physical-chemical conditions. The majority of modern serpentinites
81 form at slow and ultraslow spreading ridges during mantle unroofing and exhumation
82 at the seafloor at temperatures varying from 500 °C to <100 °C (e.g., Mével, 2003;
83 Barnes et al., 2009; Boudier et al., 2010; Bach et al., 2011; Rouméjon et al., 2018).
84 Carbonation reactions resulting in the formation of veins and ophicarbonates (i.e.,
85 carbonated ultramafic breccias resulting from repeated tectonic and/or hydraulic
86 fracturing of serpentinites) are usually associated with late stages of low-temperature
87 alteration near the seafloor (Bonatti et al., 1974; Mével, 2003; Früh-Green et al.,
88 2004; Manatschal and Müntener, 2009). Serpentinization of the subcontinental mantle
89 is also documented at ocean-continent transition (OCT) boundaries (e.g., Iberia-
90 Newfoundland rifted margins) where seawater infiltration is favored by crustal
91 thinning and tectonic activity (e.g., Boillot et al., 1989; Skelton and Valley, 2000;
92 Manatschal and Müntener, 2009; Schwarzenbach et al., 2013; Alt et al., 2018; Picazo
93 et al., 2019). In addition to passive margins, serpentinization and carbonation of
94 peridotite also occur at active margins and on continental settings. Ultramafic rocks
95 exposed in ophiolitic terrains can undergo further hydration and carbonation due to
96 low-temperature (<50 °C) interaction with meteoric water (e.g., Barnes and O’Neil,
97 1969; Barnes et al., 1978; Neal and Stanger, 1985; Streit et al., 2012; Barnes et al.,
98 2013; Falk et al., 2016).

99 The study of ophiolitic terrains is fundamental to unravel the magmatic, tectonic
100 and hydrothermal evolution of ocean basins from rift-drift and seafloor spreading
101 stages to subduction initiation and final closure (Dilek and Furnes, 2014). In fact,

102 ophiolites represent an analogue for present-day oceanic crust and preserve the only
103 evidence for ocean basins older than ~170 Ma (Dilek and Furnes, 2014; Pearce,
104 2014). Ophiolites provide better access than the one-dimensional drill cores from
105 modern oceanic crust, but they often record intense alteration during their passage
106 from rift to subduction/collision zone to mountain belt (Pierce, 2014; Staudigel et al.,
107 2014). Constraining *P-T* conditions and fluid sources of hydration and carbonation
108 reactions in ultramafic rocks from ophiolitic terrains is also important for better
109 characterizing the conditions that favor dissolution and precipitation of carbonate
110 minerals in these lithologies, with implications for better estimating the potential for
111 permanent storage of CO₂ in ultramafic rocks (Kelemen and Matter, 2008; Kelemen
112 et al., 2011). It is also crucial for tracing the mobilization and fluxes of water, carbon
113 and fluid-mobile elements among Earth's different reservoirs (e.g., Scambelluri et al.,
114 2004; Alt et al., 2012; Collins et al., 2015) and the production of fluids enriched in
115 hydrogen, methane and other hydrocarbons both at near-surface conditions (Kelley et
116 al., 2005; Miller et al., 2016) and in subduction zones (Vitale Brovarone et al., 2017).

117 Oxygen isotopes have been extensively used as geothermometers and tracers to
118 determine the temperatures and fluid sources during peridotite hydration and
119 carbonation in various tectonic settings (e.g., Wenner and Taylor, 1971, 1973;
120 Agrinier and Cannat, 1997; Früh-Green et al., 1990, 1996; Barnes et al., 2009; Lafay
121 et al., 2017; Noël et al., 2018; Rouméjon et al., 2018; Scicchitano et al., 2018a,b,
122 2020). This method requires knowledge of mineral-fluid or mineral-mineral oxygen
123 isotope fractionation factors and assumption that isotope equilibrium between co-
124 precipitated minerals and fluids was achieved and preserved. Measured $\delta^{18}\text{O}$ values in
125 co-precipitated minerals can, then, be combined with corresponding calibrations of
126 oxygen isotope fractionations to independently calculate both the equilibrium

127 temperature and the oxygen isotope composition of the interacting fluid. Several
128 studies (e.g., Wenner and Taylor, 1971; O'Hanley and Offler, 1992; Früh-Green et al.,
129 1996; Alt and Shanks, 2006; Barnes et al., 2009) have estimated serpentinization
130 temperatures and fluid $\delta^{18}\text{O}$ values using the equilibrium oxygen isotope fractionation
131 between coexisting serpentine and magnetite previously separated from the rock.
132 Geothermometry in carbonated serpentinites has recently been achieved using
133 carbonate clumped isotope techniques that allow calculating equilibrium temperatures
134 independently of the isotopic composition of the fluids from which carbonate formed
135 (e.g., Streit et al., 2012; Falk and Kelemen, 2015; de Obeso and Kelemen, 2018).
136 Studies based on mineral separates and clumped isotope techniques represent a
137 fundamental achievement in our understanding of the temperatures at which
138 serpentinization and carbonation of ultramafic rocks occur. Nevertheless, they likely
139 represent average estimates and overlook the larger complexity of these reactions
140 recorded at the microscale by the occurrence of multiple serpentine and carbonate
141 generations. In fact, recent *in situ* oxygen isotope studies by Secondary Ion Mass
142 Spectrometry (SIMS) in serpentinites and carbonated serpentinites from different
143 tectonic settings have shown a significant variation in the oxygen isotope composition
144 of serpentine and carbonate minerals recorded at the microscale (Noël et al., 2018;
145 Rouméjon et al., 2018; Scicchitano et al., 2018a, 2020). The high spatial resolution of
146 SIMS techniques allows the analysis of oxygen isotopes to be measured along
147 detailed traverses through co-precipitated host rock and vein minerals that are in
148 textural equilibrium at scales $\leq 50 \mu\text{m}$ (Turnier et al., 2020). Consequently, it is a
149 powerful tool for obtaining independent estimates of serpentinization temperatures
150 and fluid $\delta^{18}\text{O}$ values framed in a petrological context in rocks that record multiple
151 stages of fluid-rock interactions (e.g., Scicchitano et al., 2018b, 2020) as well as for

152 testing the achievement of isotopic equilibrium during serpentinization processes
153 (e.g., Lafay et al., 2019).

154 In this study we apply SIMS techniques in combination with new reference
155 materials (Scicchitano et al., 2020) to analyze oxygen and carbon isotopes in
156 serpentine, carbonate (calcite, dolomite) and magnetite in order to unravel the
157 complex fluid-rock history recorded at the microscale in ophicarbonates samples from
158 the Chenaillet ophiolite. The fine-grained textures observed in the investigated
159 samples can only be targeted by SIMS, which requires the use of matrix-matched
160 reference materials (Valley and Kita, 2009). The new analytical capabilities provide
161 unique constraints on oceanic hydrothermal alteration recorded in the Chenaillet
162 ophiolite that were not resolved by earlier studies based on conventional data.
163 Furthermore, the ability to target mineral phases that are in textural equilibrium (e.g.,
164 serpentine-carbonate, serpentine-magnetite) allowed us to constrain independently
165 both alteration temperatures and fluid sources.

166

167 **2. GEOLOGICAL SETTING AND PREVIOUS STUDIES**

168

169 The Chenaillet ophiolite in the Franco-Italian Alps (Fig. 1) is interpreted as a
170 remnant of embryonic oceanic crust formed at the distal part of a Magma-Poor-Ocean
171 Continent Transition (MP-OCT) margin (Manatschal and Müntener, 2009;
172 Manatschal et al., 2011; Li et al., 2013; Lafay et al., 2017) resembling actual slow
173 spreading centers (Lagabriele and Cannat, 1990; Lagabriele and Lemoine, 1997). It
174 consists mainly of pillow lavas with Mid Ocean Ridge Basalt (MORB) geochemical
175 signature superimposed on tectonically exhumed gabbros and serpentinized mantle
176 rocks comparable to oceanic core complexes (OCC) exposed in modern slow- to

177 ultraslow-spreading ridges (Manatschal and Müntener, 2009; Manatschal et al., 2011;
178 Li et al., 2013; Lafay et al., 2017). Recent U–Pb zircon ages in the gabbros suggest
179 that the Piemonte-Liguria oceanic domain formed between 158-166 Ma (Li et al.,
180 2013). No sheeted dike complex and post-rift sedimentary cover are observed in the
181 Chenaillet ophiolite; sediments occur locally and consist of reworked mafic and
182 ultramafic rocks covered by pelagic deposits, radiolarite and limestones (Lemoine et
183 al., 1983; Manatschal et al., 2011). In contrast to other ophiolitic terrains in the Alps,
184 the Chenaillet ophiolite escaped high-pressure metamorphism during the Late
185 Cretaceous to Eocene Alpine subduction and was only weakly overprinted by
186 subgreenschist to lower greenschist facies metamorphism during thrusting onto the
187 European margin (Mével et al., 1978; Goffé et al., 2004; Manatschal and Müntener,
188 2009; Manatschal et al., 2011). High- to low-temperature hydrothermal processes in
189 the Chenaillet ophiolite occurred in an oceanic setting prior to obduction and are
190 represented by mylonitized amphibole-bearing gabbros (Mével et al., 1978),
191 serpentinites and ophicarbonates (Manatschal and Müntener, 2009; Lafay et al.,
192 2017). Serpentinization of mantle rocks is pervasive and original silicate minerals
193 from the igneous stage are usually replaced by mesh and bastite textures typical of
194 seafloor alteration under static conditions (Andreani et al., 2007; Manatschal and
195 Müntener, 2009; Manatschal et al., 2011; Lafay et al., 2017). The pioneering work of
196 Lemoine et al. (1983) and Lagabrielle and Lemoine (1997) has been recently
197 reconsidered by Lafay et al. (2017) who provided a detailed petrological, geochemical
198 and stable isotope (O, C, H) study of ophicarbonates from the Chenaillet ophiolite.
199 These rocks consist of few tens of meter thick layers (Fig. 1b) of breccia found atop
200 massive serpentinites near the serpentinite-basalt transition. Ophicarbonate breccias
201 are made of slightly rounded serpentinite clasts cemented by a matrix of small (~12

202 μm in average) calcite grains (Lemoine et al., 1983; Lafay et al., 2017) (Fig. A.1). The
203 diversity of microstructures (veins, replacement, matrix) allowed the authors to
204 identify multiple events of carbonation following initial serpentinization of
205 peridotites, which were attributed to a progressive cooling during exhumation of the
206 mantle at the seafloor (Lafay et al., 2017). However, values of $\delta^{18}\text{O}$ in serpentine (3.3
207 to 5.1‰) and carbonates (11 to 16‰) could suggest that both serpentinization and
208 carbonation occurred at higher temperatures ($T = 155\text{-}190\text{ }^{\circ}\text{C}$ and $110\text{-}180\text{ }^{\circ}\text{C}$,
209 respectively) than seafloor alteration (Lafay et al., 2017). These temperature estimates
210 should be reexamined. They were calculated assuming a constant unaltered seawater
211 composition (Lafay et al., 2017) and homogenous mineral grains. However, the
212 microstructures and chemical zoning suggest that the micro-drilling technique used to
213 select serpentine and carbonate for stable isotope analyses has mixed different
214 generations resulting in average compositions. In light of recent analytical
215 developments allowing accurate *in situ* analysis of oxygen and carbon isotopes in
216 serpentine, magnetite and carbonate by SIMS (Valley and Kita, 2009; Huberty et al.,
217 2010; Kita et al., 2011; Śliwiński et al., 2015a,b; Scicchitano et al., 2018a, 2020), a
218 number of ophicarbonates studied by Lafay et al. (2017) were reanalyzed for stable
219 isotope ratios (O, C) by SIMS to: (i) target the various serpentine and carbonate
220 generations identified by Lafay et al. (2017) that could not be separated with micro-
221 drilling techniques due to their fine-grained size, (ii) identify systematic isotopic
222 zoning recorded at the microscale in both serpentine and carbonate, (iii) couple *in situ*
223 analysis of oxygen isotopes in potentially co-crystallized minerals (serpentine-calcite,
224 serpentine-dolomite, calcite-dolomite, serpentine-magnetite) to estimate the
225 equilibrium temperature independently of the fluid composition. To the best of our
226 knowledge, this study represents the first successful attempt to applying the

227 serpentine-magnetite geothermometer at the microscale and provides the first stable
228 isotope data in dolomite in these samples that could not be targeted by previous
229 studies due to its small grain size.

230

231 **3. PREPARATION OF GRAIN MOUNTS AND ANALYTICAL METHODS**

232

233 Five ophicarbonates samples (RL3, RL6, RL7, RL9 and RL10) from the Chenaillet
234 ophiolite previously characterized by Lafay et al. (2017) were prepared for oxygen
235 and carbon isotope analysis by SIMS, as described in the Electronic Appendix A.

236 A Hitachi S3400 Variable Pressure (VP) Scanning Electron Microscope (SEM) at
237 the Department of Geoscience (University of Wisconsin-Madison, UW-Madison) was
238 operated at low ($P = 30$ Pa) and high vacuum in backscattered electron (BSE) mode to
239 identify the different generations of serpentine, carbonate and magnetite in the
240 Chenaillet ophicarbonates described by Lafay et al. (2017). Carbonate minerals were
241 also imaged using a cathodoluminescence (CL) Gatan PanaCL/F system. Careful
242 SEM imaging in BSE, secondary electron (SE) and CL modes was performed
243 following each SIMS session to check the location and features of all SIMS pits. We
244 rejected analyses where pits were located on fractures, mixed domains or other
245 features that could alter isotope ratios. Prior to SEM analysis, mounts were coated
246 with carbon or a thin layer of gold; to avoid affecting carbon isotope ratios during
247 SIMS analysis in carbonates, no carbon coating was used on the corresponding
248 mounts. The accelerating voltage and working distance were usually ~ 15 or 10 kV
249 and ~ 10 or 15 mm for BSE and CL imaging, respectively.

250 Serpentine, calcite, dolomite and magnetite from the Chenaillet ophicarbonates
251 were analyzed for major and minor element mineral chemistry using a CAMECA

252 SXFive Field Emission Electron Microprobe (EPMA) at the Department of
253 Geoscience (UW-Madison). Details of EPMA methods are given in the Electronic
254 Appendix A. Direct analysis of oxygen with EPMA was necessary for accurate
255 quantification of variable Fe oxidation in serpentine and magnetite and variable water
256 contents in serpentine. All serpentine analyses were normalized to 18 (O + OH)
257 according to the general formula $Mg_6Si_4O_{10}(OH)_8$. Approximate H₂O content (wt.%)
258 was calculated based on excess oxygen values measured by EPMA assuming total
259 iron as Fe²⁺ (Table A.1). Carbonate analyses were normalized to 6 O according to the
260 general formula (Ca,Mg)₂(CO₃)₂ (Table A.2). Magnetite analyses were normalized to
261 3 cations according to the general formula Fe₃O₄, and approximate Fe³⁺ and Fe²⁺
262 contents were estimated by charge balance (Table A.3).

263 A CAMECA IMS-1280 large radius multicollector secondary ion mass
264 spectrometer at the WiscSIMS laboratory (UW-Madison) was used to perform *in situ*
265 oxygen and carbon isotope analyses of serpentine, carbonate and magnetite in the
266 Chenaillet ophicarbonates during seven analytical sessions (Tables A.1 to A.4).
267 Details on analytical settings are given in the Electronic Appendix A. We monitored
268 bias, drift and external precision during each analytical session by bracketing 10-20
269 unknown analyses with at least eight analyses of the reference material located in the
270 same grain mount. Matrix effects on bias due to variations in Mg/Fe ratios in
271 serpentine and dolomite-ankerite solid solutions, which are observed during oxygen
272 and carbon isotope analysis by SIMS (Śliwiński et al., 2015a,b; Scicchitano et al.,
273 2020), were monitored and quantified for each analytical session by constructing a
274 calibration curve using a suite of serpentine and carbonate reference materials (Table
275 A.4). These calibration curves were then used to correct $\delta^{18}O$ and $\delta^{13}C$ values
276 measured in serpentine and dolomite from the Chenaillet ophicarbonates. Orientation

277 effects in chrysotile were estimated by analyzing two different orientations of the
278 chrysotile C22908 reference material as described in Scicchitano et al. (2018a, 2020),
279 while orientation effects in magnetite were minimized using a special 3 kV protocol
280 (see Electronic Appendix A for details) and evaluated by analyzing ~30 grains with
281 different orientation of the magnetite M7-5830 reference material (Huberty et al.,
282 2010; Kita et al., 2011).

283

284

4. RESULTS

285

286 4.1. Petrography and mineral chemistry

287

288 For the purpose of this study, we summarize the main textures targeted for *in situ*
289 analysis by SIMS, which are essential for putting into petrological context the new
290 oxygen and carbon isotope data.

291

292 4.1.1. Serpentine

293

294 Serpentine is the main constituent of the serpentinite clasts where it forms either
295 mesh textures characterized by well-defined cores and rims (Fig. 2a-c) or hourglass
296 textures in which a distinction between mesh rim and mesh center is not possible (Fig.
297 2d). Raman spectroscopy showed that mesh cores consist of a mixture between
298 lizardite and chrysotile (hereafter referred to as “serpentine”), whereas mesh rims
299 consist of pure lizardite (Lafay et al., 2017). Magnetite (up to ~20 μm large) is often
300 observed around mesh cores in sample RL6 (Fig. 2b), while it is usually lacking or
301 very limited in mesh textures of other samples. It is occasionally possible to identify

302 an inner and outer mesh core both surrounded by magnetite (Fig. 2b). A complex
303 network of mesh veinlets (V-1) consisting of lizardite+magnetite follows original
304 (pristine silicate) grain boundaries (Fig. 2e-f), while larger lizardite+magnetite veins
305 250 μm in width (V-2) crosscut mesh and hourglass textures (Fig. 2g). In sample
306 RL6, lizardite+dolomite layers are observed within the carbonate matrix (Fig. 2j-k);
307 this serpentine generation is hereafter referred to as “matrix serpentine”. Finally,
308 small chrysotile aggregates up to a few tens of μm large (Lafay et al., 2017) are
309 widespread in the carbonate matrix surrounding serpentinite clasts (Fig. 2k-l).

310 Mesh cores have higher Mg numbers [$\text{Mg\#} = 100 \times \text{Mg}/(\text{Mg}+\text{Fe})$, molar, with Fe
311 = Fe(total)] and silica contents relative to mesh rims in all samples (Fig. A.2). In
312 particular, mesh cores in samples RL6, RL7 and RL9 have Mg# ranging between 96
313 and 99 mole % and SiO_2 contents ranging between 40.6 and 43.4 wt.%, whereas mesh
314 rims have Mg# of 90 to 97 mole % and SiO_2 contents of 38.0 to 42.0 wt.% (Fig. A.2,
315 Table A.1). A similar trend between Mg# and silica is observed in mesh textures from
316 samples RL10 and RL3, which however show lower Mg# (91 to 95 mole % in mesh
317 cores, 85 to 95 mole % in mesh rims) and comparable SiO_2 contents (39.9 to 42.5
318 wt.% in mesh cores, 36.0 to 42.8 wt.% in mesh rims) relative to mesh serpentine in
319 the other three samples (Fig. A.2, Table A.1). The variability in alumina content is
320 lower in mesh serpentine from samples RL6, RL7 and RL9 ($\text{Al}_2\text{O}_3 = 0.2\text{-}1.3$ wt.%)
321 relative to mesh serpentine from samples RL10 and RL3 ($\text{Al}_2\text{O}_3 = 0.1\text{-}4.3$ wt.%) (Fig.
322 A.2, Table A.1). Serpentine in hourglass textures has a similar chemical composition
323 as serpentine in mesh rims (Fig. A.2, Table A.1). Lizardite in V-1 veins has similar
324 silica ($\text{SiO}_2 = 41.2\text{-}43.1$ wt.%) and alumina contents ($\text{Al}_2\text{O}_3 = 0.1\text{-}0.6$ wt.%) across
325 different samples, whereas Mg# decreases from sample RL9 (Mg# = 96-97) to
326 samples RL10 and RL3 (Mg# = 94-95) (Fig. A.2, Table A.1). Lizardite in V-2 veins

327 and “matrix serpentine” observed in sample RL6 have similar chemical compositions
328 as those of mesh cores in the same sample (Fig. A.2, Table A.1). Chrysotile in the
329 carbonate matrix surrounding serpentinite clasts is also characterized by higher Mg#
330 in samples RL6, RL7 and RL9 (Mg# = 94-98) relative to samples RL10 and RL3
331 (Mg# = 88-95; Fig. A.2, Table A.1); in contrast, both silica and alumina contents are
332 similar across different samples ($\text{SiO}_2 = 39.5\text{-}44.2$ wt.%, $\text{Al}_2\text{O}_3 = 0.2\text{-}2.2$ wt.%).

333

334 **4.1.2. Carbonates within serpentinite clasts**

335

336 Serpentine in mesh cores is often partially or completely replaced by calcite
337 (hereafter referred to as C2, Lafay et al., 2017) and relict serpentine inclusions are
338 frequently observed in calcite mesh (Fig. 2a-c). C2 calcite is sometimes connected to
339 calcite veinlets ~ 10 μm in width (hereafter C1; Lafay et al., 2017); the largest C1
340 calcite veins (up to 500 μm in width) crosscut serpentine in mesh and hourglass
341 textures as well as V-1 and V-2 lizardite+magnetite veins (Fig. 2h-i). Although C1
342 calcite veins are usually restricted to individual clasts and are often truncated at the
343 edges of the clasts, they sometimes propagate into the surrounding carbonate matrix
344 (Fig. A.1). SEM-CL imaging shows complex patchy zoning and resorption features in
345 both C1 veins and C2 mesh suggesting multiple events of recrystallization (Fig. 3). As
346 previously shown by Lafay et al. (2017), the edges of C1 calcite veins are sometimes
347 delimited by distinct CL calcite rims (Fig. 3b-c).

348 In addition to calcite, subordinate dolomite is observed in some samples as (i) rims
349 around C2 calcite mesh (Fig. 3e, 4a), (ii) borders along C1 veins at the boundary with
350 serpentine (Fig. 3a, 4b), (iii) subhedral grains associated with “matrix serpentine” in
351 sample RL6 (Fig. 2k, 4c) and (iv) veinlets in the C3 calcite matrix.

352 No significant variation is observed in the chemical composition of calcite in
353 different textures across different samples (Table A.2). FeO and MnO contents are
354 usually <0.5 wt.% with the exception of calcite in C2 mesh (FeO = 0.1-1.3 wt.%)
355 from sample RL6. In contrast, the MgO content in calcite from different textures has a
356 larger variability from 0.02 to 1.6 wt.% (Table A.2).

357 Dolomite has a similar chemical composition in all samples and textural locations
358 with FeO content varying from 0.1 to 1.2 wt.% and MnO content <0.3 wt.%; Fe# is
359 <3 mole %.

360

361 **4.1.3. Carbonates surrounding serpentinite clasts**

362

363 Serpentinite clasts are embedded in a calcite matrix (hereafter C3; Lafay et al.,
364 2017) that appears either “turbid”, when intergrown with fine-grained chrysotile
365 aggregates as documented through Raman spectroscopy (Lafay et al., 2017), or
366 “clear”, when no chrysotile is present (Fig. A.3). Clear calcite domains (hereafter
367 C1’) in the C3 calcite matrix were interpreted by Lafay et al. (2017) as remnants of
368 C1 veins channeling fluids. Calcite veins ~100 µm in width (hereafter C3-veins)
369 sometimes crosscut the C3 calcite matrix but not the lizardite+dolomite layers (Fig.
370 2j). Finally, a large calcite vein ~5 mm in width (hereafter C4; Lafay et al., 2017)
371 crosscuts both C3 calcite matrix and serpentinite clasts in sample RL9 (Fig. A.1).
372 SEM-CL imaging shows that C1’ clear calcite domains consist of large calcite grains
373 that sometimes exhibit a concentric (Fig. 5a-b) or oscillatory CL zoning (Fig. 5c)
374 truncated by the surrounding aggregates of fine-grained C3 calcite matrix; the latter
375 also shows a similar concentric CL zoning (Fig. 5a, d). Calcite grains in C1’ are often
376 crosscut or bounded by later calcite veinlets (hereafter C1’-veins) (Fig. 5a, c). In

377 contrast, C3-veins do not exhibit complex CL zoning (Fig. 5d). In addition to calcite,
378 dolomite was observed at the boundary between C4 vein and serpentinite clast in
379 sample RL9 (Fig. 4d).

380 FeO and MnO contents are usually <0.5 wt.% with the exception of calcite in C3-
381 veins (MnO = 0.1-0.7 wt.%) from sample RL6. In contrast, the MgO content in
382 calcite from different textures has a larger variability from 0.03 to 1.9 wt.% (Table
383 A.2). No significant variation is observed between different textures across different
384 samples.

385

386 **4.2. Oxygen and carbon isotopes by SIMS**

387

388 **4.2.1. Serpentine**

389

390 *In situ* oxygen isotope analyses of serpentinite were performed in two analytical
391 sessions (S1 and S2; Table A.1). A suite of six (S1) to seven (S2) antigorite reference
392 materials was analyzed at the beginning of each analytical session in order to build a
393 calibration curve for the correction of polymorph-specific matrix effects due to Mg/Fe
394 variations in the compositional range Mg# = 77.5-99.5 (Table S2 in Scicchitano et al.,
395 2020). Lizardite (L3431) and chrysotile (C22908) reference materials (Scicchitano et
396 al., 2018a, 2020) were also analyzed to correct for the bias relative to the normalizing
397 antigorite reference material Al06-44A (Table S2 in Scicchitano et al., 2020). A bias
398 of ~1‰ was measured between lizardite L3431 and antigorite Al06-44A in both
399 analytical sessions. Orientation effects in chrysotile C22908 were ~1‰ in all
400 analytical sessions, hence this is considered as a limitation on the accuracy of
401 analyses done in this polymorph, but no orientation effects are detected for lizardite or

402 antigorite. Measured $\delta^{18}\text{O}$ values in serpentine from the Chenaillet ophicarbonates
403 were corrected according to the method described in Scicchitano et al. (2020) and are
404 reported relative to the V-SMOW scale (Table A.1).

405 The highest average $\delta^{18}\text{O}$ values are recorded in the core of mesh textures where
406 oxygen isotope ratios vary between 4.4 and 8.5‰ with no distinction between calcite-
407 free and calcite-bearing mesh cores (Fig. 6). Although mesh rims show a large
408 variability in oxygen isotope ratios with $\delta^{18}\text{O}$ values varying from 4.5 to 8.8‰, their
409 average $\delta^{18}\text{O}$ values are generally lower compared to mesh cores (Fig. 6). No
410 correlation between $\delta^{18}\text{O}$ value and Mg# was observed in mesh textures. Lizardite in
411 V-1 veins has an oxygen isotope composition varying from 3.5 to 6.4‰ with average
412 $\delta^{18}\text{O}$ values lower relative to mesh rims (Fig. 6). Lizardite in V-2 veins crosscutting
413 both V-1 veins and mesh textures has low $\delta^{18}\text{O}$ values of 3.2-4.2‰ (Fig. 6). Similar
414 low oxygen isotope ratios relative to mesh cores are recorded in hourglass serpentine
415 ($\delta^{18}\text{O} = 3.8\text{-}5.7\text{‰}$), “matrix serpentine” ($\delta^{18}\text{O} = 3.1\text{-}5.4\text{‰}$) and serpentine in the C4
416 calcite vein ($\delta^{18}\text{O} = 4.0\text{-}4.8\text{‰}$) (Fig. 6). Chrysotile in the C3 calcite matrix has a large
417 variability in $\delta^{18}\text{O}$ values from 3.0 to 5.7‰ (Fig. 6).

418 Overall, SIMS analyses allow identifying a larger variation in serpentine $\delta^{18}\text{O}$
419 values (from 3.0 to 8.8‰) relative to previous studies on powdered micro-drilled
420 samples ($\delta^{18}\text{O} = 3.3\text{-}5.1\text{‰}$; Lafay et al., 2017) as well as a systematic variation in
421 $\delta^{18}\text{O}$ values between different serpentine generations.

422

423 **4.2.2. Carbonate**

424

425 *In situ* oxygen and carbon isotope analyses in carbonates were performed in four
426 analytical sessions (S3 to S5 for O, S6 for C; Table A.2). Calcite UWC-3 (Kozdon et

427 al., 2009) was used as a working reference material. A suite of seven to ten carbonate
428 reference materials was analyzed at the start of each session to calibrate matrix effects
429 in samples with chemical composition along the dolomite-ankerite solid solution
430 series (Table A.4). Measured $\delta^{18}\text{O}$ and $\delta^{13}\text{C}$ values in dolomite from the Chenaillet
431 ophicarbonates were corrected according to the method described in Śliwiński et al.
432 (2015a,b) and for the bias between dolomite UW6220 and calcite UWC-3 reference
433 materials (Table A.2). Values of $\delta^{18}\text{O}$ and $\delta^{13}\text{C}$ are reported relative to the V-SMOW
434 and V-PDB scales, respectively (Table A.2).

435 Values of $\delta^{18}\text{O}$ for calcite in C1 veins mostly range between 9.4 and 13.9‰ and
436 occasionally up to 22.3‰ (Fig. 7). The highest $\delta^{18}\text{O}$ values are commonly observed at
437 the edges of large C1 veins (Fig. 3b). Analyses performed across one of the largest C1
438 veins (Fig. 3c, A.4a) showed a nearly symmetric edge-to-edge oxygen isotope zoning
439 up to ~3‰ with the lowest $\delta^{18}\text{O}$ values in the core of the vein (Fig. A.4). Values of
440 $\delta^{13}\text{C}$ for C1 calcite veins vary between -0.6 and 2.4‰ but no systematic correlation is
441 observed with textures (Fig. A.5). Calcite in C2 mesh textures shows the largest
442 variability in oxygen isotope composition with $\delta^{18}\text{O}$ values ranging from 9.8 to
443 30.6‰ (Fig. 7), whereas $\delta^{13}\text{C}$ values vary between -2.6 and 1.9‰ (Fig. A.5). The
444 highest $\delta^{18}\text{O}$ values in C2 calcite mesh are typically observed at the core of mesh
445 textures, whereas the edges usually have lower $\delta^{18}\text{O}$ values (Fig. 3d-i). It is sometimes
446 possible to observe resorption textures where calcite with low $\delta^{18}\text{O}$ values, similar to
447 those measured in nearby C1 veinlets, replaces C2 calcite mesh cores with higher
448 $\delta^{18}\text{O}$ values (Fig. 3f-i). Calcite in C1' textures also shows a large variability in oxygen
449 and carbon isotopes similar to C2 calcite mesh with $\delta^{18}\text{O}$ and $\delta^{13}\text{C}$ values of 10.6 to
450 24.9‰ and -1.1 to 1.6‰, respectively (Fig. 7, A.5). Similar to calcite in C2 mesh
451 textures, the highest $\delta^{18}\text{O}$ values in C1' textures are commonly observed in the cores

452 of large calcite grains (Fig. 5 and Electronic Appendix B). Late C1'-veins
453 crosscutting or bounding C1' calcite grains have low $\delta^{18}\text{O}$ values of 10.9 to 11.8‰
454 (Fig. 5c, 7 and Electronic Appendix B) and $\delta^{13}\text{C}$ values of -0.6 to 0.7‰ (Fig. A.5).
455 Similarly, calcite in the fine-grained C3 matrix and crosscutting C3-veins also have
456 low $\delta^{18}\text{O}$ values of 9.8-12.9‰ and 10.5-11.5‰, respectively (Fig. 5d, 7 and B.1 in
457 Electronic Appendix B); $\delta^{13}\text{C}$ values vary from -0.1 to 2.2‰ and -0.6 to 0.6‰ ,
458 respectively (Fig. A.5). Finally, calcite in the latest C4 vein has the highest average
459 oxygen isotope composition (average $\delta^{18}\text{O} = 21.1\text{‰}$, Fig. 7) and carbon isotope
460 values similar to calcite in other textural locations ($\delta^{13}\text{C} = -0.7$ to 1.7‰ , Fig. A.5).
461 Dolomite associated with mesh textures in serpentinite clasts has $\delta^{18}\text{O}$ values of 10.7
462 to 14.1‰ ($n = 20$) that are comparable to the oxygen isotope composition of dolomite
463 bordering C1 calcite veins ($\delta^{18}\text{O} = 10.1$ -11.9‰, $n = 9$) and the C4 vein ($\delta^{18}\text{O} = 11.2$ -
464 12.5‰, $n = 2$) (Table A.2). Similar $\delta^{18}\text{O}$ values are also recorded in subhedral
465 dolomite associated with matrix serpentine in the layers at the boundary between
466 serpentinite clasts and C3 calcite matrix ($\delta^{18}\text{O} = 11.4$ -13.2‰, $n = 5$) (Table A.2).
467 SIMS analyses show a much larger variability ($\sim 21\text{‰}$) in calcite $\delta^{18}\text{O}$ values
468 relative to $\sim 6\text{‰}$ variation described in Lafay et al. (2017). Additionally, the ability to
469 place SIMS data into a petrological context highlights that higher $\delta^{18}\text{O}$ values in
470 zoned C1 veins, C2 mesh and C1' calcite domains likely represent an older signature
471 that is progressively replaced by younger calcite generations with lower $\delta^{18}\text{O}$ values
472 (core of C1 veins, C1'-veins, C3 matrix and C3-veins). SEM-CL imaging linked to
473 oxygen isotope ratios also allowed distinguishing C1' domains from C1 open veins.
474 Values of $\delta^{18}\text{O}$ increase again in the latest C4 calcite vein (average $\delta^{18}\text{O} = 21.1\text{‰}$)
475 crosscutting serpentinite clasts and C3 calcite matrix (average $\delta^{18}\text{O} = 11.1\text{‰}$). Values
476 of $\delta^{13}\text{C}$ measured by SIMS vary by $\sim 4.5\text{‰}$ at most in C2 calcite mesh, similar to the

477 variation observed by Lafay et al. (2017). Nevertheless, SIMS analyses are generally
478 higher relative to those reported in Lafay et al. (2017) (−2.6 to +2.4‰ vs. −5.2 to
479 +0.4‰, respectively).

480

481 **4.2.3. Magnetite**

482

483 *In situ* oxygen isotope analyses in magnetite were performed in one analytical
484 session (S7; Table A.3). The extent of crystal orientation effects in magnetite was
485 determined by bracketing analyses of the M7-5830 magnetite reference material with
486 eight analyses of the UWQ-1 quartz reference material (Kelly et al., 2007) (Table
487 A.4). A grain-to-grain reproducibility of ~1‰ (2 standard deviations, 2SD) was
488 obtained (using the low-kV protocol of Kita et al., 2011) in both M7-5830 and UWQ-
489 1 (Table A.4); hence this represents the maximum precision achievable during oxygen
490 isotope analyses of magnetite in this study. Magnetite analyses in the ophicarbonates
491 samples from the Chenaillet ophiolite were bracketed with eight analyses in the
492 UWC-3 calcite reference material (Kozdon et al., 2009) located in the same grain
493 mounts in order to monitor bias, drift and external precision (Table A.3). Magnetite
494 analyses were corrected for the bias between UWC-3 calcite and M7-5830 magnetite
495 reference materials measured in different mounts, and they are reported relative to the
496 V-SMOW scale (Tables A.3 and A.4).

497 Magnetite grains larger than ~10 µm located in different textures (mesh, V-1 and
498 V-2 veins, hourglass serpentine) were targeted for SIMS oxygen isotopes analysis in
499 samples RL6, RL3 and RL9 (Table A.3). Magnetite in mesh textures (Fig. 2b and
500 A.6a) shows the largest variability in $\delta^{18}\text{O}$ values from −10.6 to −5.0‰ ($n = 32$).
501 Magnetite in V-1 veins (Fig. 2f and A.6b) and V-2 veins (Fig. 2g and A.6c) has

502 oxygen isotope ratios varying from -8.5 to -7.3‰ ($n = 3$) and -7.7 to -10.6‰ ($n = 2$),
503 respectively. Magnetite associated with hourglass serpentine (Fig. 2d and A.6d) has
504 an oxygen isotope composition of -9.6 to -8.0‰ ($n = 4$).

505

506

5. DISCUSSION

507

508 **5.1. Estimating alteration temperatures and water $\delta^{18}\text{O}$ values in co-crystallized** 509 **mineral pairs**

510

511 Based on textural observations, we identified seven pairs of minerals that appear to
512 be in textural equilibrium along the metasomatic sequence and, therefore, assumed to
513 have co-crystallized: (i) lizardite+magnetite in mesh textures with a single mesh core,
514 V-1 veins (Fig. 2e, f), V-2 veins (Fig. 2g), and in the hourglass matrix (Fig. 2d); (ii)
515 lizardite+dolomite in the layers at the boundary between serpentinite clast and
516 carbonate matrix (Fig. 2k and 4c) as well as with hourglass serpentine (Fig. 4b, d);
517 (iii) chrysotile+calcite in the C3 calcite matrix (Fig. 2l). Coupled oxygen isotope
518 analysis by SIMS in these mineral pairs allows us to test whether isotopic equilibrium
519 was achieved during hydration and carbonation reactions, in which case equilibrium
520 temperatures and water $\delta^{18}\text{O}$ values are independently estimated.

521

522 **5.1.1. Serpentine-magnetite**

523

524 The majority of targeted serpentine-magnetite pairs ($n = 17$, Table 1) are in mesh
525 textures (sample RL6) because of the larger ($>10\ \mu\text{m}$) size of magnetite grains. Only a

526 limited number of analyses was possible in V-1 veins ($n = 1$), V-2 veins ($n = 2$) and
527 hourglass matrix ($n = 4$) because of the small grain size of magnetite (Table 1).

528 A large uncertainty exists on the serpentine-water oxygen isotope fractionation
529 because different calibrations (Wenner and Taylor, 1971; Savin and Lee, 1988; Früh-
530 Green et al., 1996; Zheng, 1993; Saccocia et al., 2009) disagree by $>4\text{‰}$ and up to
531 $\sim 20\text{‰}$ when extrapolated to temperatures $<200\text{ °C}$ (see Fig. 10 and discussion in
532 Scicchitano et al., 2020). In this study, the preferred calibrations for calculating the
533 equilibrium temperature for each serpentine-magnetite pair are the serpentine-water
534 oxygen isotope fractionation factors of Früh-Green et al. (1996) and the magnetite-
535 water oxygen isotope fractionation factors of Bottinga and Javoy (1973). The same
536 calibrations were then used to calculate the oxygen isotope composition of water in
537 equilibrium with both serpentine and magnetite at each equilibrium temperature
538 (Table 1 and Fig. 8). For mesh cores, equilibrium temperatures vary from 204 °C to
539 132 °C and $\delta^{18}\text{O}_{(\text{water})}$ values decrease with temperature from 5.2 to 1.8‰ (Fig. 8). For
540 serpentine-magnetite pairs in V-1 veins, V-2 veins and hourglass textures, equilibrium
541 temperatures vary from 173 °C , $169\text{-}215\text{ °C}$ and $162\text{-}198\text{ °C}$, respectively, while
542 water $\delta^{18}\text{O}$ values vary between ~ 1 and 3‰ (Fig. 8).

543 For comparison, equilibrium temperatures and $\delta^{18}\text{O}_{(\text{water})}$ values were also
544 calculated using other calibrations. Estimates calculated by combining the serpentine-
545 water oxygen isotope fractionation factors of Saccocia et al. (2009) with the
546 magnetite-water oxygen isotope fractionation factors of Bottinga and Javoy (1973)
547 differ by $\sim 50\text{ °C}$ (from 261 to 191 °C) and $\sim 1\text{‰}$ (from ~ 4 to 0‰), respectively,
548 relative to estimates derived from the calibration by Früh-Green et al. (1996) (Fig. 8
549 and Table 1). Temperatures calculated with the calibration of Saccocia et al. (2009)
550 could be overestimated of up to 40 °C (at exchange fraction $< 40\%$) due to a bias in

551 their serpentine-water calibration resulting from extrapolation of equilibrium
552 fractionation factors in three-exchange site systems using the methods described by
553 Northrop and Clayton (1966) or Zheng et al. (1994), which are valid for two-
554 exchange site systems (Agrinier and Javoy, 2016). Equilibrium temperatures
555 calculated by combining the serpentine-water and magnetite-water oxygen isotope
556 fractionation factors of Zheng (1991, 1993) as well as the serpentine-magnetite
557 calibration by Früh-Green et al. (1996; their Eq. 3) are ~50-70 °C lower than those
558 estimated using the serpentine-water and magnetite-water calibrations by Früh-Green
559 et al. (1996) and Bottinga and Javoy (1973) (Table A.5). Considering the maximum
560 uncertainties derived from the various calibration equations and $\delta^{18}\text{O}$ measurements,
561 we estimate a total uncertainty of ± 80 °C on the calculated equilibrium temperatures.
562 The uncertainty on $\delta^{18}\text{O}_{(\text{water})}$ values is estimated to be in the order of $\pm 1\%$.

563

564 **5.1.2. Serpentine-dolomite**

565

566 Lizardite and subhedral dolomite grains in the layers at the boundary between
567 serpentinite clast and carbonate matrix are relatively homogenous in oxygen isotopes
568 with average $\delta^{18}\text{O}$ values of $4.7 \pm 1.4\%$ (2SD, $n = 10$) and $12.2 \pm 1.3\%$ (2SD, $n = 5$),
569 respectively, suggesting that they are in isotopic equilibrium. Using the average $\delta^{18}\text{O}$
570 values measured by SIMS, we calculated an oxygen isotope fractionation ($\Delta^{18}\text{O}_{\text{Dol-Srp}}$)
571 of 7.5‰, which corresponds to an equilibrium temperature of 229 °C (Fig 9a). In
572 order to calculate the temperature at which serpentine and dolomite formed, we used
573 the empirical calibration of the serpentine-water oxygen isotope fractionation by
574 Früh-Green et al. (1996) and the calibration of the dolomite-water oxygen isotope
575 fractionation (experiments at $T = 252\text{-}292$ °C, Matthews and Katz, 1977).

576 Extrapolation of the experimental calibration by Saccocia et al. (2009) would result
577 in an unrealistically high equilibrium temperature (even if accounting for the bias
578 described by Agrinier and Javoy, 2016) given a maximum calculated $\Delta^{18}\text{O}_{\text{Dol-Srp}}$ of
579 5.6‰ is obtained assuming $T = 500\text{ }^\circ\text{C}$, which is the maximum thermal stability of
580 serpentine in oceanic settings (e.g., Mével, 2003). Consequently, we consider
581 extrapolation of the empirical calibration by Fröh-Green et al. (1996) more reliable.
582 At a temperature of $229\text{ }^\circ\text{C}$, serpentine and dolomite would be in equilibrium with a
583 fluid of 3.3‰ (Fig. 9b). Similar equilibrium temperature of $240\text{ }^\circ\text{C}$ and water $\delta^{18}\text{O}$
584 value of 3.3‰ are calculated using the average oxygen isotope ratios measured in
585 hourglass serpentine and dolomite pairs (Table 2, Fig. 9). These estimates are within
586 uncertainty of those calculated for lizardite+magnetite pairs in hourglass textures.
587

588 **5.1.3. Serpentine-calcite**

589

590 Calcite in the fine-grained C3 matrix and the co-crystallized fine-grained chrysotile
591 have average $\delta^{18}\text{O}$ values of $11.1 \pm 1.2\text{‰}$ (2SD, $n = 57$) and $3.9 \pm 1.4\text{‰}$ (2SD, $n = 22$),
592 respectively, corresponding to a $\Delta^{18}\text{O}_{\text{Cal-Srp}}$ of 7.2‰ (Fig. 9a). Combining the
593 empirical calibration of the serpentine-water system by Fröh-Green et al. (1996) with
594 the experimental calibration of the calcite-water oxygen isotope fractionation
595 (experiments at $T = 0\text{-}500\text{ }^\circ\text{C}$, O'Neil et al., 1969), yields an equilibrium temperature
596 of $208\text{ }^\circ\text{C}$ and a $\delta^{18}\text{O}_{(\text{water})}$ of 2.0‰ (Fig. 9). The calibration by O'Neil et al. (1969) is
597 in good agreement with experimental calibrations by Golyshev et al. (1981) and Kim
598 and O'Neil (1997). As for the dolomite-serpentine pair, the experimental calibration
599 by Saccocia et al. (2009) for the calcite-serpentine pair would result in unrealistically

600 high equilibrium temperature not consistent with seafloor serpentinization ($T > 500$
601 °C).

602

603 **5.2. Evolution model for the hydrothermal alteration in the Chenaillet ophiolite**

604

605 In the following discussion, stable isotope data are combined with petrographic
606 observations and well-documented geological context to reconstruct the main phases
607 of fluid-rock interaction recorded in the Chenaillet ophiocarbonates (Fig. 10, 11).

608 Alteration temperatures and water oxygen isotope compositions estimated
609 independently from mineral-mineral pairs (see above) are used as anchor points for
610 the interpretations.

611

612 **5.2.1. Exhumation to the seafloor: early serpentinization followed by low- T** 613 **carbonation**

614

615 Oxygen isotope values of serpentine increase from V-1 mesh veins ($\delta^{18}\text{O} = 3.5$ to
616 6.4‰) to mesh cores ($\delta^{18}\text{O} = 4.4$ to 8.5‰), with no distinction between carbonate-free
617 and carbonate-bearing mesh textures (Fig. 6, 10). Additionally, serpentine in mesh
618 textures associated with magnetite has similar oxygen isotope and chemical
619 compositions as serpentine in magnetite-free mesh textures from the same sample.

620 Hence, we assume that the formation of serpentine in different mesh cores (i.e.,
621 magnetite- and calcite-bearing versus magnetite- and calcite-free) is attributable to the
622 same hydrothermal event. The physical-chemical conditions at which serpentine in V-
623 1 mesh veins and mesh rims formed cannot be independently constrained, but it is
624 likely that they record the earliest stages of alteration with V-1 veins acting as

625 conduits that allowed progressive fluid percolation and pervasive replacement in
626 mesh cores. The variation in Mg# and Al₂O₃ observed in mesh textures from samples
627 RL6, RL7 and RL9 versus samples RL10 and RL3 (Fig. A.2) suggests formation of
628 serpentine after olivine versus pyroxene, respectively (e.g., Deschamps et al., 2013).
629 Because no relict pyroxene and olivine are observed in any of the investigated
630 samples, it is possible that serpentinization started at $T > 400$ °C (favoring rapid
631 dissolution of orthopyroxene) and then proceeded at $T < 300$ °C (favoring rapid
632 dissolution of olivine), as documented by experimental studies (e.g., Martin and Fyfe,
633 1970; Allen and Seyfried, 2003). The limited occurrence of antigorite, chlorite and
634 tremolite in the Chenaillet ophicarbonates (Lafay et al., 2017) is consistent, in fact,
635 with greenschist facies conditions ($T = 300$ - 500 °C). The abundant precipitation of
636 massive magnetites in mesh cores would explain the formation of serpentine with
637 higher Mg# in response to changes in the conditions of hydrothermal alteration. It
638 should be noted that the marked crystallization of magnetite in mesh cores could be a
639 consequence of the combined variation in fluid temperature and $\delta^{18}\text{O}$ composition,
640 water/rock ratio (W/R) and redox conditions (Klein et al., 2009, 2013).

641 In light of the above assumptions, the physical-chemical conditions at which the
642 serpentine-magnetite pairs in mesh textures formed (i.e., $T = 204$ to 132 °C and
643 $\delta^{18}\text{O}_{(\text{water})} = 5$ to 2‰) can be considered valid for serpentine in all mesh cores. It is
644 worth noting that the concomitance between cooling and decrease in water $\delta^{18}\text{O}$
645 values results in a net variation of magnetite and serpentine $\delta^{18}\text{O}$ values by $\sim 5.5\text{‰}$
646 and $\sim 0.4\text{‰}$, respectively (Fig. A.7); this is consistent with the variability in $\delta^{18}\text{O}$
647 values measured by SIMS in serpentine-magnetite pairs (Table 1). The decrease in
648 fluid $\delta^{18}\text{O}$ values during cooling is consistent with a progressive evolution from a
649 rock-dominated system during early stages of serpentinization (or low W/R), with

650 water $\delta^{18}\text{O}$ values similar to the oxygen isotopic composition of the upper mantle
651 ($\delta^{18}\text{O}_{\text{mantle}} = 5.5\text{‰}$, $\delta^{18}\text{O}_{\text{olivine}} = 5.18 \pm 0.28\text{‰}$; e.g., Matthey et al., 1994; Chazot et al.,
652 1997), to a fluid-dominated system during later stages of serpentinization (or high
653 W/R) and exhumation of the mantle near the seafloor. Calculated water $\delta^{18}\text{O}$ values of
654 $\sim 2\text{‰}$ agree well with $\delta^{18}\text{O}$ values of 1.2-1.5‰ (Logatchev hydrothermal field) and
655 2.2-2.4‰ (Nibelungen hydrothermal field) measured in hot ($T = 192\text{-}365^\circ\text{C}$)
656 ultramafic-hosted vent fluids sampled along the Mid-Atlantic slow-spreading ridge
657 (e.g., Charlou et al., 2010 and references therein; Schmidt et al., 2011), which are
658 higher in $\delta^{18}\text{O}$ than present-day pure seawater (0‰) due to interaction with the
659 oceanic crust (e.g., Mével, 2003). Similar temperatures ($T = 265\text{-}364^\circ\text{C}$) and $\delta^{18}\text{O}$
660 values (1.1-2.4‰) are also recorded in mafic-hosted vent fluids (e.g., Jean-Baptiste et
661 al., 1997).

662 Our new *in situ* data are overall in agreement with the original suggestion of Lafay
663 et al. (2017) who, in continuity with the tectonic models proposed by Manatschal et
664 al. (2011), proposed that exhumation of oceanic units occurred along detachment
665 faults favoring hydration and carbonation of mantle rocks (Fig. 12a). The authors
666 proposed that serpentinization initiated in a shallow seafloor environment at
667 conditions of at least 150°C , with reactive fluids assumed to have $\delta^{18}\text{O}$ values of 0-
668 2‰. The new *in situ* data suggest comparable temperature estimates within
669 uncertainty, but independently constrain the composition and origin of the interacting
670 fluids as well as identify that early serpentinization was followed by early low-
671 temperature carbonation due to exposure of the mantle rocks on the paleo seafloor and
672 interaction with low-temperature seawater (Fig. 12a). This is documented by the
673 zonation in $\delta^{18}\text{O}$ values observed in some carbonate generations (Fig. 7, 10), with
674 texturally older calcite domains having high $\delta^{18}\text{O}$ values in zoned C2 calcite mesh

675 (18.0-30.6‰), at the edges of zoned C1 veins (18.7-22.3‰) and in the cores of zoned
676 C1' domains (18.2-24.9‰), which are comparable to those reported for marine
677 carbonates and metacarbonates from the Lago Nero unit (Lemoine et al., 1983). Such
678 carbonates likely formed at temperatures as low as 10 °C assuming interaction with
679 pure seawater in an ice-free world ($\delta^{18}\text{O} = -1\text{‰}$). Such low carbonation temperatures
680 relative to serpentinization are also consistent with the observation that calcite in
681 mesh textures is clearly replacing (hence postdating) serpentine.

682

683 **5.2.2. An active hydrothermal cell: coupled high-*T* carbonation and** 684 **serpentinization**

685

686 An overall decrease in oxygen isotope values with textural progression is recorded
687 by both serpentine and carbonate in all investigated samples (Fig. 6, 7, 10). In
688 particular, $\delta^{18}\text{O}$ values of serpentine in V-2 veins ($\delta^{18}\text{O} = 3.2\text{-}4.2\text{‰}$) and hourglass
689 textures ($\delta^{18}\text{O} = 3.8\text{-}5.7\text{‰}$) are $\sim 3\text{‰}$ lower on average relative to serpentine in mesh
690 cores (Fig. 6). Similarly, texturally younger calcite in zoned C2 mesh, C1 veins and
691 C1' domains has $\delta^{18}\text{O}$ values down to $\sim 10\text{‰}$ (Fig. 7, 10). Low oxygen isotope ratios
692 are also recorded in lizardite at the boundary between serpentinite clast and carbonate
693 matrix ($\delta^{18}\text{O} = 3.1\text{-}5.4\text{‰}$), chrysotile intergrown with fine-grained C3 calcite ($\delta^{18}\text{O} =$
694 $3.0\text{-}5.7\text{‰}$), C3 calcite matrix ($\delta^{18}\text{O} = 9.8\text{-}12.8\text{‰}$), C3-veins ($\delta^{18}\text{O} = 10.7\text{-}11.4\text{‰}$) and
695 C1'-veins ($\delta^{18}\text{O} = 10.9\text{‰}$). Oxygen isotope thermometry from mineral pairs (see
696 above) suggests that such a drop in $\delta^{18}\text{O}$ values in both serpentine and carbonates is
697 consistent with a crystallization temperature of up to 240 °C and water $\delta^{18}\text{O}$ value of
698 $2\pm 1\text{‰}$. The smooth oxygen isotope zoning in both C1 veins and C1' domains as well
699 as the similarity in fluid $\delta^{18}\text{O}$ compositions between early and late stages of

700 hydrothermal alteration point to a continuous process that likely occurred entirely in a
701 seafloor environmental setting. The pervasive carbonation textures often overprint
702 serpentinization ones, but we do not exclude that carbonation initiated while residual
703 anhydrous silicates were still present. The calculated oxygen isotope compositions of
704 water are consistent with isotopically shifted seawater rather than indicative of
705 interaction with meteoric water or metamorphic fluids in continental settings. Oxygen
706 isotope values measured in serpentine fall in the range of oceanic serpentinites
707 (Wenner and Taylor, 1973) and all values of $\delta^{13}\text{C}$ in carbonates (from -2.6 to $+2.4\%$)
708 suggest a seawater origin for carbon. It is worth noting that in a $\delta^{18}\text{O}$ versus $\delta^{13}\text{C}$ plot,
709 the carbonates from the Chenaillet ophiolite show a distinct horizontal trend parallel
710 to the $\delta^{18}\text{O}$ axis (Fig. A.5) suggesting that the fraction of CO_2 in the fluid was not
711 significant. Calcite can precipitate at a mole fraction of $\text{CO}_2/(\text{CO}_2 + \text{H}_2\text{O})$ as low as
712 0.01, but in such case a high water/rock ratio is required for a significant carbonation.
713 Carbonate cements commonly form at low temperature from seawater (biogenic and
714 abiogenic) and freshwater (calcretes and speleothems). High- $\delta^{18}\text{O}$ carbonates are
715 assumed to form in equilibrium with very low- T seawater and our new thermometry
716 estimates suggest that low- $\delta^{18}\text{O}$ carbonates in the Chenaillet ophicarbonates formed at
717 high temperature. Consequently, both temperature and water $\delta^{18}\text{O}$ must have changed.
718 The flat trend can result from the dissolution and reprecipitation of pre-existing
719 carbonates that interacted with nearly pure water such that the $\delta^{13}\text{C}$ remained
720 constant. This agrees with observations of dissolution and reprecipitation textures in
721 the carbonates of the investigated samples.

722 Heating associated with burial during oceanic spreading is an unlikely scenario to
723 explain this high- T hydrothermal event due to the intense fracturing of the
724 ophicarbonates that points to active tectonics, accordingly to Lafay et al. (2017) who

725 also suggested that authigenic carbonation, partially replacing serpentinites and
726 achieving mantle minerals alteration, occurred under brittle conditions favored by the
727 likely fluid-dominated system and tectonic context. In fact, the authors hypothesized
728 that the composition of the fluid and the temperature conditions evolved in a
729 hydrothermal environment comparable to that observed in the vicinity of mid-ocean
730 hydrothermal vents, i.e. active tectonic and magmatic conditions. The occurrence of a
731 warmer (200-240 °C) stage of hydrothermal alteration due to interaction with evolved
732 seawater-derived fluids ($\delta^{18}\text{O} = 2\text{-}3\text{‰}$) documented by the new *in situ* data could be
733 the result of burial by lavas causing reheating and channeling of upwelling
734 hydrothermal fluids along high-angle faults (Fig. 12b). Such a scenario would be
735 consistent with the tectonic models of Manatschal et al. (2011) for the Chenaillet
736 ophiolite suggesting that a first stage of mantle exhumation along a detachment fault
737 was followed by a stage of ‘high-angle extrusion’, when magma and fluids were
738 remobilized along high-angle faults acting also as feeder channels for the overlying
739 pillow basalts. A similar model of high-temperature hydrothermal discharge, driven
740 by mafic intrusions, along normal faults lying at high angle to an oceanic detachment
741 surface was proposed by Alt et al. (2018) in the northern Appenine ophiolites. The
742 authors documented an evolution of the fault system at the paleo-seafloor from talc
743 alteration and sulfide deposits, typical of high-temperature hydrothermal discharge (T
744 ≈ 350 °C), to carbonated serpentinites formed at $T \approx 100$ °C (Alt et al., 2018).
745 Carbonates formed at temperatures as high as ~ 225 °C are observed also in the
746 serpentinite basement of the Lost City Hydrothermal Field in the Mid-Atlantic Ridge,
747 where they precipitate from warm hydrothermal fluids with high concentrations of
748 methane and hydrogen derived from serpentinization (Früh-Green et al., 2003).
749

750 **5.2.3. Late stage veining**

751

752 The youngest C4 calcite vein records a large variability in $\delta^{18}\text{O}$ values (12.3 to
753 23.9‰) and the highest average oxygen isotope composition among different
754 carbonate generations (Fig. 7). No independent calculations of temperature and fluid
755 oxygen isotope composition are possible due to the lack of mineral pairs. It is,
756 therefore, necessary to assume that the variation in $\delta^{18}\text{O}$ values is due to a variation in
757 temperature, fluid oxygen isotope composition or more likely a combination of both.
758 Given the lowest $\delta^{18}\text{O}$ values are comparable to those measured in the “high-
759 temperature” carbonates, it is plausible that formation of the C4 vein started in similar
760 physical-chemical conditions and continued due to interaction with progressively
761 cooler and low- $\delta^{18}\text{O}$ hydrothermal fluids (down to a minimum of ~ 40 °C, assuming
762 $\delta^{18}\text{O}_{(\text{water})}$ of -1 ‰) due to mixing with fresh seawater channeled along fractures at
763 shallower depths. Such estimates are comparable, for instance, to the active vent
764 fluids sampled at the Lost City Hydrothermal Field characterized by low temperature
765 ($T = 55\text{-}75$ °C) and $\delta^{18}\text{O}$ values (0-0.1‰), and are interpreted to result from mixing
766 between seawater and high-pH fluids derived from subsurface serpentinization
767 reactions (Früh-Green et al., 2003). The evolutionary model suggested here for the
768 hydrothermal alteration of the Chenaillet ophicarbonates is consistent with the overall
769 observation that this ophiolitic terrain was only partly affected by low-grade
770 metamorphism during obduction.

771

772

6. CONCLUSIONS

773

774 We performed *in situ* analysis by SIMS of oxygen and carbon isotopes in
775 serpentine, calcite, dolomite and magnetite from ophicarbonates from the
776 Chenaillet ophiolitic complex (western Alps). SIMS analysis revealed unprecedented
777 zoning in oxygen isotope ratios of serpentine (3.0 to 8.8‰), calcite (9.4 to 30.6‰)
778 and magnetite (−5.0 to −10.6‰) relative to previous studies, which relied on
779 conventional bulk analysis. To the best of our knowledge, we document the first
780 evidence of ‘cold carbonates’ (i.e., carbonates with $\delta^{18}\text{O} > 25\text{‰}$; e.g., Fig. 6 in Picazo
781 et al., 2020 and references therein) in Alpine ophiolites. The lack of such high oxygen
782 isotope signatures in other Alpine ophiolitic terrains could be due to the much larger
783 sampling scale of the bulk techniques that average $\delta^{18}\text{O}$ values of multiple mineral
784 generations. The high spatial resolution of SIMS allowed direct quantification of
785 oxygen isotope ratios in mineral pairs that are in textural equilibrium and are
786 interpreted to have co-crystallized. The relative oxygen isotope homogeneity of the
787 targeted mineral pairs is consistent with isotopic equilibrium allowing for the
788 independent calculation of equilibrium temperatures and water oxygen isotope values.
789 Considering that the temperature–pressure stabilities of serpentine minerals are not
790 well constrained, *in situ* stable isotope thermometry presents a powerful tool to
791 constrain the conditions at which alteration of ultramafic rocks occurs in various
792 tectonic settings. Additionally, numerical models by Klein and Garrido (2011) show
793 that temperature-dependent activity gradients of both aqueous carbon dioxide
794 ($a_{\text{CO}_2,\text{aq}}$) and aqueous silica ($a_{\text{SiO}_2,\text{aq}}$) determine the carbonation potential of
795 serpentinite. Independently constraining the formation temperature is therefore
796 essential to estimating $a_{\text{SiO}_2(\text{aq})}$, $a_{\text{CO}_2(\text{aq})}$, oxygen fugacity and pH, which in turn
797 would allow estimating the phase equilibria with implications for the monitoring of
798 reaction progress during CO_2 sequestration of ultramafic rocks (Klein and Garrido,

799 2011). Nevertheless, a major source of uncertainty on the calculation of alteration
800 temperatures, particularly for the serpentine-water system, remains the large
801 discrepancy between different calibrations of the oxygen isotope fractionation at $T <$
802 $200\text{ }^{\circ}\text{C}$, hence future studies should aim to improve such calibrations. The new
803 dataset and thermometry estimates in the Chenaillet ophiolite are interpreted as
804 indicative of a continuous hydrothermal alteration starting during uplift and exposure
805 of the lithospheric mantle to the seafloor, subsequently followed by further
806 carbonation and serpentinization induced by hot (up to $240\text{ }^{\circ}\text{C}$) and isotopically
807 shifted ($\delta^{18}\text{O} \sim 2\text{‰}$) seawater, and finally by channeling of and mixing with low- T and
808 low- $\delta^{18}\text{O}$ seawater along fractures. This scenario is consistent with alteration
809 occurring in long-lived hydrothermal systems controlled by tectonic activity where
810 multiple metasomatic events can explain effective mantle hydration and carbonation
811 over a few tens of thousands of years. Carbonation of ultramafic rocks in oceanic
812 settings plays an important role for the global carbon cycle as abyssal peridotites and
813 serpentinites might act as a sink for CO_2 . Unraveling the complexity and sequence of
814 reactions, temperatures and fluid compositions responsible for peridotite or
815 serpentinite carbonation in oceanic and continental settings is important for correctly
816 estimating rates of mineral carbonation and potential for CO_2 intake.

817

818

ACKNOWLEDGEMENTS

819

820 We thank Mike Spicuzza and Brian Hess for assistance with sample
821 preparation, Bil Schneider and John Fournelle for assistance with SEM and EPMA
822 analyses, Kouki Kitajima for assistance in the SIMS lab and data processing. We are
823 grateful to Eugenio Piluso for fruitful discussions and for reading an earlier version of

824 the manuscript. Jeffrey Alt, Frieder Klein and an anonymous reviewer are
825 acknowledged for constructive reviews that helped improve the manuscript. We also
826 thank Frieder Klein for editorial handling. This work is supported by the U.S.
827 Department of Energy, Office of Science, Office of Basic Energy Sciences
828 (Geosciences) under Awards Number DE-FG02-93ER14389 and DE-SC0020666.
829 WiscSIMS is supported by the U.S. National Science Foundation (EAR-1658823, -
830 2004618) and the University of Wisconsin- Madison.

REFERENCES

- 831
832
- 833 Agrinier P. and Cannat M. (1997) Oxygen-isotope constraints on serpentinization
834 processes in ultramafic rocks from the mid-atlantic ridge (23°N). *Proc. Ocean*
835 *Drill. Program, Sci. Results* **153**, 381–388.
836 doi:10.2973/odp.proc.sr.153.033.1997
- 837 Agrinier P. and Javoy M. (2016) Unbiased isotope equilibrium factors from partial
838 isotope exchange experiments in 3-exchange site systems. *Geochim. Cosmochim.*
839 *Acta* **189**, 197–213.
- 840 Allen D. E and Seyfried W. E. (2003) Compositional controls on vent fluids from
841 ultramafic-hosted hydrothermal systems at mid-ocean ridges: An experimental
842 study at 400 °C, 500 bars. *Geochim. Cosmochim. Acta* **67**, 1531–1542.
- 843 Alt J. C. and Shanks W. C. (2006) Stable isotope compositions of serpentinite
844 seamounts in the Mariana forearc: Serpentinization processes, fluid sources and
845 sulfur metasomatism. *Earth Planet. Sci. Lett.* **242**, 272–285.
846 doi:10.1016/j.epsl.2005.11.063
- 847 Alt J. C., Garrido C. J., Shanks W. C., Turchyn A., Padrón-Navarta J. A., López
848 Sánchez-Vizcaíno V., Gómez Pugnaire M. T. and Marchesi C. (2012) Recycling
849 of water, carbon, and sulfur during subduction of serpentinites: A stable isotope
850 study of Cerro del Almirante, Spain. *Earth Planet. Sci. Lett.* **327–328**, 50–60.
851 doi:10.1016/j.epsl.2012.01.029
- 852 Alt J., Crispini L., Gaggero L., Levine D., Lavagnino G., Shanks P. and Gulbransen
853 C. (2018) Normal faulting and evolution of fluid discharge in a Jurassic seafloor
854 ultramafic-hosted hydrothermal system. *Geology* **46**, 523–526.
- 855 Andreani M., Mével C., Boullier A. M. and Escartín J. (2007) Dynamic control on

856 serpentine crystallization in veins: Constraints on hydration processes in oceanic
857 peridotites. *Geochemistry, Geophys. Geosystems* **8**, doi:10.1029/2006GC001373

858 Bach W., Rosner M., Jöns N., Rausch S., Robinson L. F., Paulick H. and Erzinger J.
859 (2011) Carbonate veins trace seawater circulation during exhumation and uplift
860 of mantle rock: Results from ODP Leg 209. *Earth Planet. Sci. Lett.* **311**, 242–
861 252. doi:10.1016/j.epsl.2011.09.021

862 Barnes I. and O’Neil J. R. (1969) The relationship between fluids in some fresh
863 Alpine-type ultramafics and possible modern serpentinization, Western United
864 States. *Geol. Soc. Am. Bull.* **80**, 1947–1960.

865 Barnes I., O’Neil J. R. and Trescases J. J. (1978) Present day serpentinization in New
866 Caledonia, Oman and Yugoslavia. *Geochim. Cosmochim. Acta* **42**, 144–145.

867 Barnes J. D., Paulick H., Sharp Z. D., Bach W. and Beaudoin G. (2009) Stable isotope
868 ($\delta^{18}\text{O}$, δD , $\delta^{37}\text{Cl}$) evidence for multiple fluid histories in mid-Atlantic abyssal
869 peridotites (ODP Leg 209). *Lithos* **110**, 83–94. doi:10.1016/j.lithos.2008.12.004

870 Barnes J. D., Eldam R., Lee C.-T. A., Errico J. C., Loewy S. and Cisneros M. (2013)
871 Petrogenesis of serpentinites from the Franciscan Complex, western California,
872 USA. *Lithos* **178**, 143–157. doi:10.1016/j.lithos.2012.12.018

873 Boillot G., Féraud G., Recq M. and Girardeau J. (1989) Undercrusting by serpentinite
874 beneath rifted margins. *Nature* **341**, 523–525.

875 Bonatti E., Emiliani C., Ferrara G., Honnorez J. and Rydell H. (1974) Ultramafic-
876 carbonate breccias from the equatorial mid atlantic ridge. *Mar. Geol.* **16**, 83–102.

877 Bottinga Y. and Javoy M. (1973) Comments on oxygen isotope geothermometry.
878 *Earth Planet. Sci. Lett.* **20**, 250–265.

879 Boudier F., Baronnet A. and Mainprice D. (2010) Serpentine Mineral Replacements
880 of Natural Olivine and their Seismic Implications: Oceanic Lizardite versus

881 Subduction-Related Antigorite. *J. Petrol.* **51**, 495–512.
882 doi:10.1093/petrology/egp049

883 Charlou J. L., Donval J. P., Konn C., Ondréas H. and Fouquet Y. (2010) High
884 production and fluxes of H₂ and CH₄ and evidence of abiotic hydrocarbon
885 synthesis by serpentinization in ultramafic-hosted hydrothermal systems on the
886 Mid-Atlantic Ridge. In *Diversity of hydrothermal systems on slow spreading*
887 *ocean ridges* (eds. P. A. Rona, C. W. Devey, J. Dymant and B. J. Murton),
888 *American Geophysical Union* **188**, 265–296.

889 Chazot G., Lowry D., Menzies M. and Matthey D. (1997) Oxygen isotopic
890 composition of hydrous and anhydrous mantle peridotites. *Geochim.*
891 *Cosmochim. Acta* **61**, 161–169.

892 Collins N. C., Bebout G. E., Angiboust S., Agard P., Scambelluri M., Crispini L. and
893 John T. (2015) Subduction zone metamorphic pathway for deep carbon cycling:
894 II. Evidence from HP/UHP metabasaltic rocks and ophicarbonates. *Chem. Geol.*
895 **412**, 132–150. doi:10.1016/j.chemgeo.2015.06.012

896 de Obeso J. C. and Kelemen P. B. (2018) Fluid rock interactions on residual mantle
897 peridotites overlain by shallow oceanic limestones: Insights from Wadi Fins,
898 Sultanate of Oman. *Chem. Geol.* **498**, 139–149.
899 doi:10.1016/j.chemgeo.2018.09.022

900 Deschamps F., Godard M., Guillot S. and Hattori K. (2013) Geochemistry of
901 subduction zone serpentinites: A review. *Lithos* **178**, 96–127.
902 doi:10.1016/j.lithos.2013.05.019

903 Dilek Y. and Furnes H. (2014) Ophiolites and their origins. *Elements* **10**, 93–100.

904 Falk E. S. and Kelemen P. B. (2015) Geochemistry and petrology of listvenite in the
905 Samail ophiolite, Sultanate of Oman: Complete carbonation of peridotite during

906 ophiolite emplacement. *Geochim. Cosmochim. Acta* **160**, 70–90.
907 doi:10.1016/j.gca.2015.03.014

908 Falk E. S., Guo W., Paukert A. N., Matter J. M., Mervine E. M. and Kelemen P. B.
909 (2016) Controls on the stable isotope compositions of travertine from
910 hyperalkaline springs in Oman: Insights from clumped isotope measurements.
911 *Geochim. Cosmochim. Acta* **192**, 1–28. doi:10.1016/j.gca.2016.06.026

912 Früh-Green G. L., Weissert H. and Bernoulli D. (1990) A multiple fluid history
913 recorded in Alpine ophiolites. *J. Geol. Soc. London* **147**, 959–970.
914 doi:10.1144/gsjgs.147.6.0959

915 Früh-Green G. L., Plas A. and Lecuyer C. (1996) Petrologic and Stable Isotope
916 Constraints on Hydrothermal Alteration and Serpentinization of the EPR
917 Shallow Mantle at Hess Deep (Site 895). *Proc. Ocean Drill. Program, 147 Sci.*
918 *Results* **147**, doi:10.2973/odp.proc.sr.147.016.1996

919 Früh-Green G. L., Connolly J. A. D., Plas A., Kelley D. S. and Grobety B. (2004)
920 Serpentinization of the oceanic peridotites: Implication for geochemical cycles
921 and biological activity. *Geophys. Monogr. Ser.* **144**, 119–136.

922 Goffé B., Schwartz S., Lardeaux J. M. and Bousquet R. (2004) Metamorphic structure
923 of the Western and Ligurian Alps. *Mitt. Osterr. Miner. Ges.* **149**, 125–144.

924 Golyshev S. I., Padalko N. I. and Pechenkin S. A. (1981) Fractionation of stable
925 isotopes in carbonate systems. *Geochem. Int'l.* **10**, 85–99.

926 Huberty J. M., Kita N. T., Kozdon R., Heck P. R., Fournelle J. H., Spicuzza M. J., Xu
927 H. and Valley J. W. (2010) Crystal orientation effects in $\delta^{18}\text{O}$ for magnetite and
928 hematite by SIMS. *Chem. Geol.* **276**, 269–283.

929 Jean-Baptiste P., Charlou J. L. and Stievenard M. (1997) Oxygen isotope study of
930 mid-ocean ridge hydrothermal fluids: Implication for the oxygen-18 budget of

931 the oceans. *Geochim. Cosmochim. Acta* **61**, 2669–2677.

932 Kelemen P. B. and Matter J. (2008) In situ carbonation of peridotite for CO₂ storage.
933 *Proc. Natl. Acad. Sci.* **105**, 17295–17300.

934 Kelemen P. B., Matter J., Streit E. E., Rudge J. F., Curry W. B. and Blusztajn J.
935 (2011) Rates and Mechanisms of Mineral Carbonation in Peridotite: Natural
936 Processes and Recipes for Enhanced, in situ CO₂ Capture and Storage. *Annu.*
937 *Rev. Earth Planet. Sci.* **39**, 545–576. doi:10.1146/annurev-earth-092010-152509

938 Kelley D. S., Karson J. A., Früh-Green G. L., Yoerger D. R., Shank T. M., Butterfield
939 D. A., Hayes J. M., Schrenk M. O., Olson E. J., Proskurowski G., Jakuba M.,
940 Bradley A., Larson B., Ludwig K., Glickson D., Buckman K., Bradley A. S.,
941 Brazelton W. J., Roe K., Bernasconi S. M., Elend M. J., Lilley M. D., Baross J.
942 A., Summons R. E. and Sylva S. P. (2005) A Serpentinite-Hosted Ecosystem:
943 The Lost City Hydrothermal Field. *Science* **307**, 1428–1435.

944 Kelly J. L., Fu B., Kita N. T. and Valley J. W. (2007) Optically continuous silcrete
945 quartz cements of the St. Peter Sandstone: High precision oxygen isotope
946 analysis by ion microprobe. *Geochim. Cosmochim. Acta* **71**, 3812–3832.
947 doi:10.1016/j.gca.2007.05.014

948 Kim S.-T. and O’Neil J. R. (1997) Equilibrium and nonequilibrium oxygen isotope
949 effects in synthetic carbonates. *Geochim. Cosmochim. Acta* **61**, 3461–3475.

950 Kita N. T., Huberty J. M., Kozdon R., Beard B. L. and Valley J. W. (2011) High
951 precision SIMS oxygen, sulfur and iron stable isotope analyses of geological
952 materials: Accuracy, surface topography and crystal orientation. SIMS XVII
953 Proceedings, *Surface and Interface Analysis* **43**, 427-431, DOI 10.1002/sia.3424.

954 Klein F. and Garrido C. J. (2011) Thermodynamic constraints on mineral carbonation
955 of serpentinized peridotite. *Lithos* **126**, 147–160.

- 956 Klein F., Bach W., Jöns N., McCollom T., Moskowitz B. and Berquó T. (2009) Iron
957 partitioning and hydrogen generation during serpentinization of abyssal
958 peridotites from 15 N on the Mid-Atlantic Ridge. *Geochim. Cosmochim. Acta*
959 **73(22)**, 6868–6893.
- 960 Klein F., Bach W. and McCollom T. M. (2013) Compositional controls on hydrogen
961 generation during serpentinization of ultramafic rocks. *Lithos* **178**, 55–69.
- 962 Kozdon R., Ushikubo T., Kita N. T., Spicuzza M. and Valley J. W. (2009) Intratest
963 oxygen isotope variability in the planktonic foraminifer *N. pachyderma*: Real vs.
964 apparent vital effects by ion microprobe. *Chem. Geol.* **258**, 327–337.
965 doi:10.1016/j.chemgeo.2008.10.032
- 966 Lafay R., Baumgartner L. P., Schwartz S., Picazo S., Montes-Hernandez G. and
967 Vennemann T. (2017) Petrologic and stable isotopic studies of a fossil
968 hydrothermal system in ultramafic environment (Chenaillet ophiolites,
969 Western Alps, France): Processes of carbonate cementation. *Lithos* **294–295**,
970 319–338. doi:10.1016/j.lithos.2017.10.006
- 971 Lafay R., Baumgartner L. P., Putlitz B. and Siron G. (2019) Oxygen isotope
972 disequilibrium during serpentinite dehydration. *Terra Nov.* **31**, 94–101.
973 doi:10.1111/ter.12373
- 974 Lagabriele Y. and Cannat M. (1990) Alpine Jurassic ophiolites resemble the modern
975 central Atlantic basement. *Geology* **18**, 319–322.
- 976 Lagabriele Y. and Lemoine M. (1997) Alpine, Corsican and Apennine ophiolites: the
977 slow-spreading ridge model. *C. R. Acad. Sci. Ser. IIA Earth Planet. Sci.* **325**,
978 909–920.
- 979 Lemoine M., Bourbon M., Graciansky P.-C. and Létolle R. (1983) Isotopes du
980 carbone et de l'oxygène de calcaires associés à des ophiolites (Alpes Occidentales,

981 Corse, Apennin): indices possibles d'un hydrothermalisme océanique téthysien.
982 *Revue de Géologie Dynamique et de Géographie Physique* **24**, 305–314.

983 Li X.-H., Faure M., Lin W. and Manatschal G. (2013) New isotopic constraints on
984 age and magma genesis of an embryonic oceanic crust: The Chenaillet Ophiolite
985 in the Western Alps. *Lithos* **160–161**, 283–291. doi:10.1016/j.lithos.2012.12.016

986 Manatschal G. and Müntener O. (2009) A type sequence across an ancient magma-
987 poor ocean-continent transition: the example of the western Alpine Tethys
988 ophiolites. *Tectonophysics* **473**, 4–19. doi:10.1016/j.tecto.2008.07.021

989 Manatschal G., Sauter D., Karpoff A. M., Masini E., Mohn G. and Lagabriele Y.
990 (2011) The Chenaillet Ophiolite in the French/Italian Alps: An ancient analogue
991 for an Oceanic Core Complex? *Lithos* **124**, 169–184.
992 doi:10.1016/j.lithos.2010.10.017

993 Martin B. and Fyfe W. S. (1970) Some experimental and theoretical observations on
994 the kinetics of hydration reactions with particular reference to serpentinization.
995 *Chem. Geol.* **6**, 185–202.

996 Matthey D., Lowry D. and Macpherson C. (1994) Oxygen isotope composition of the
997 mantle peridotite. *Earth Planet. Sci. Lett.* **128**, 231–241.

998 Matthews A. and Katz A. (1977) Oxygen isotope fractionation during the
999 dolomitization of calcium carbonate. *Geochim. Cosmochim. Acta* **41**, 1431–
1000 1438.

1001 Mével C. (2003) Serpentinization of abyssal peridotites at mid-ocean ridges. *C. R.*
1002 *Geosci.* **335**, 825–852. doi:10.1016/j.crte.2003.08.006

1003 Mével C., Cabry R. and Kienast J.-R. (1978) Amphibolite facies conditions in the
1004 oceanic crust: example of amphibolitized flaser-gabbro and amphibolites from
1005 the Chenaillet ophiolite massif (Hautes Alpes, France). *Earth Planet. Sci. Lett.*

1006 **39**, 98–108.

1007 Miller H. M., Matter J. M., Kelemen P., Ellison E. T., Conrad M. E., Fierer N.,
1008 Ruchala T., Tominaga M. and Templeton A. S. (2016) Modern water/rock
1009 reactions in Oman hyperalkaline peridotite aquifers and implications for
1010 microbial habitability. *Geochim. Cosmochim. Acta* **179**, 217–241.
1011 doi:10.1016/j.gca.2016.01.033

1012 Neal C. and Stanger G. (1985) Past and present serpentinisation of ultramafic rocks;
1013 an example from the Semail ophiolite nappe of northern Oman. In *The Chemistry*
1014 *of Weathering* (eds. J. I. Drewer). D. Reidel Publishing Company, Holland, pp.
1015 249–275.

1016 Noël J., Godard M., Olliot E., Martinez I., Williams M., Boudier F., Rodriguez O.,
1017 Chaduteau C., Escario S. and Gouze P. (2018) Evidence of polygenetic carbon
1018 trapping in the Oman Ophiolite: Petro-structural, geochemical, and carbon and
1019 oxygen isotope study of the Wadi Dima harzburgite-hosted carbonates (Wadi
1020 Tayin massif, Sultanate of Oman). *Lithos* doi:10.1016/j.lithos.2018.08.020

1021 Northrop D. A. and Clayton R. N. (1966) Oxygen isotope fractionations in systems
1022 containing dolomite. *J. Geol.* **74**, 174–196.

1023 O’Hanley D. S. and Offler R. (1992) Characterization of multiple serpentinization,
1024 Woodsreef, New South Wales. *Can. Mineral.* **30**, 1113–1126.

1025 O’Neil J. R., Clayton R. N. and Mayeda T. K. (1969) Oxygen Isotope Fractionation in
1026 Divalent Metal Carbonates. *J. Chem. Phys.* **51**, 5547–5558.

1027 Pearce J. A. (2014) Immobile element fingerprinting of ophiolites. *Elements* **10**, 101–
1028 108.

1029 Picazo S., Lafay R., Faucheux V. and Vennemann T. (2019) New constraints on
1030 carbonation associated with brecciation in hyperextended margins (example of

1031 Iberia and Newfoundland margins). *Terra Nov.* **31**, 317–331.
1032 doi:10.1111/ter.12383

1033 Picazo S., Malvoisin B., Baumgartner L. and Bouvier Anne-Sophie (2020) Low
1034 temperature serpentinite replacement by carbonates during seawater influx in the
1035 Newfoundland Margin. *Minerals* **10**, 184. doi:10.3390/min10020184

1036 Rouméjon S., Williams M. J. and Früh-Green G. L. (2018). In-situ oxygen isotope
1037 analyses in serpentine minerals: Constraints on serpentinization during tectonic
1038 exhumation at slow- and ultraslow-spreading ridges. *Lithos* **323**, 156–173.
1039 doi:10.1016/j.lithos.2018.09.021

1040 Saccocia P. J., Seewald J. S. and Shanks W. C. (2009) Oxygen and hydrogen isotope
1041 fractionation in serpentine-water and talc-water systems from 250 to 450 °C, 50
1042 MPa. *Geochim. Cosmochim. Acta* **73**, 6789–6804. doi:10.1016/j.gca.2009.07.036

1043 Savin S. M. and Lee M. (1988) Isotopic studies of phyllosilicates. *Rev. Mineral.* **19**,
1044 189–223.

1045 Scambelluri M., Fiebig J., Malaspina N., Müntener O. and Pettke T. (2004)
1046 Serpentinite Subduction: Implications for Fluid Processes and Trace-Element
1047 Recycling. *Int. Geol. Rev.* **46**, 595–613. doi:10.2747/0020-6814.46.7.595

1048 Schmidt K., Garbe-Schönberg D., Koschinsky A., Straus H., Jost C. L., Klevenz V.
1049 and Königer P. (2011) Fluid elemental and stable isotope composition of the
1050 Nibelungen hydrothermal field (8°18'S, Mid-Atlantic Ridge): Constraints on
1051 fluid-rock interaction in heterogeneous lithosphere. *Chem. Geol.* **280**, 1–18.

1052 Schwarzenbach E. M., Früh-Green G. L., Bernasconi S. M., Alt J. C. and Plas A.
1053 (2013) Serpentinization and carbon sequestration: A study of two ancient
1054 peridotite-hosted hydrothermal systems. *Chem. Geol.* **351**, 115–133.
1055 doi:10.1016/j.chemgeo.2013.05.016

1056 Scicchitano M. R., Rubatto D., Hermann J., Shen T., Padrón-Navarta J. A., Williams
1057 I. S. and Zheng Y.-F. (2018a) In Situ Oxygen Isotope Determination in
1058 Serpentine Minerals by Ion Microprobe: Reference Materials and Applications to
1059 Ultrahigh-Pressure Serpentinites. *Geostand. Geoanalytical Res.* **42**, 459–479.
1060 doi:10.1111/ggr.12232

1061 Scicchitano M. R., Rubatto D., Hermann J., Majumdar A. S. and Putnis A. (2018b)
1062 Oxygen isotope analysis of olivine by ion microprobe: Matrix effects and
1063 applications to a serpentinitised dunite. *Chem. Geol.* **499**, 126–137.
1064 doi:10.1016/j.chemgeo.2018.09.020

1065 Scicchitano M. R., Spicuzza M. J., Ellison E. T., Tuschel D., Templeton A. S. and
1066 Valley J. W. (2020) In situ oxygen isotope determination in serpentine minerals
1067 by SIMS: Addressing matrix effects and providing new insights on
1068 serpentinitisation at Hole BA1B (Samail ophiolite, Oman). *Geostand.*
1069 *Geoanalytical Res.* **45**, 161-187. doi: 10.1111/ggr.12359

1070 Skelton A. D. L. and Valley J. W. (2000) The relative timing of serpentinitisation and
1071 mantle exhumation at the ocean-continent transition, Iberia: Constraints from
1072 oxygen isotopes. *Earth Planet. Sci. Lett.* **178**, 327–338. doi:10.1016/S0012-
1073 821X(00)00087-X

1074 Śliwiński M. G., Kitajima K., Kozdon R., Spicuzza M. J., Fournelle J. H., Denny A.
1075 and Valley J. W. (2015a) Secondary Ion Mass Spectrometry Bias on Isotope
1076 Ratios in Dolomite–Ankerite, Part I: $\delta^{18}\text{O}$ Matrix Effects. *Geostand.*
1077 *Geoanalytical Res.* **40**, 157–172. doi:10.1111/j.1751-908X.2015.00364.x

1078 Śliwiński M. G., Kitajima K., Kozdon R., Spicuzza M. J., Fournelle J. H., Denny A.
1079 and Valley J. W. (2015b) Secondary Ion Mass Spectrometry Bias on Isotope
1080 Ratios in Dolomite–Ankerite, Part II: $\delta^{13}\text{C}$ Matrix Effects. *Geostand.*

1081 *Geoanalytical Res.* **40**, 173–184. doi:10.1111/j.1751-908X.2015.00380.x

1082 Staudigel H., Furnes H. and Smits M. (2014) Deep biosphere record of in situ oceanic
1083 lithosphere and ophiolites. *Elements* **10**, 121–126.

1084 Streit E., Kelemen P. and Eiler J. (2012) Coexisting serpentine and quartz from
1085 carbonate-bearing serpentinized peridotite in the Samail Ophiolite, Oman.
1086 *Contrib. to Mineral. Petrol.* **164**, 821–837. doi:10.1007/s00410-012-0775-z

1087 Turnier R. B., Katzir Y., Kitajima K., Orland I. J., Spicuzza M. J. and Valley J. W.
1088 (2020) Calibration of oxygen isotope fractionation and calcite-corundum
1089 thermometry in emery at Naxos, Greece. *J. Metamorph. Geol.* **38**, 53–70.

1090 Valley J. W. and Kita N. T. (2009) In situ oxygen isotope geochemistry by ion
1091 microprobe. *Mineral. Assoc. Canada Short Course Ser.* **41**, 19–63.

1092 Vitale Brovarone A., Martinez I., Elmaleh A., Compagnoni R., Chaduteau C., Ferraris
1093 C. and Esteve I. (2017) Massive production of abiotic methane during
1094 subduction evidenced in metamorphosed ophicarbonates from the Italian Alps.
1095 *Nat. Commun.* **8**, 1–13. doi:10.1038/ncomms14134

1096 Wenner D. B. and Taylor H. P. (1971) Temperatures of serpentinization of ultramafic
1097 rocks based on O¹⁸/O¹⁶ fractionation between coexisting serpentine and
1098 magnetite. *Contrib. to Mineral. Petrol.* **32**, 165–185. doi:10.1007/BF00643332

1099 Wenner D. B. and Taylor H. P. (1973) Oxygen and hydrogen isotope studies of the
1100 serpentinization of ultramafic rocks in oceanic environments and continental
1101 ophiolite complexes. *Am. J. Sci.* **273**, 207–239. doi:10.2475/ajs.273.3.207

1102 Zheng Y.-F. (1991) Calculation of oxygen isotope fractionation in metal oxides.
1103 *Geochim. Cosmochim. Acta* **55**, 2299–2307.

1104 Zheng Y.-F. (1993) Calculation of oxygen isotope fractionation in hydroxyl-bearing
1105 silicates. *Earth Planet. Sci. Letters* **120**, 247–263.

1106 Zheng Y.-F., Metz P., Satir M. and Sharp Z. D. (1994) An experimental calibration of
1107 oxygen isotope fractionation between calcite and forsterite in the presence of a
1108 CO₂-H₂O fluid. *Chem. Geol.* **116**, 17–27.
1109
1110

FIGURE AND TABLE CAPTIONS

1111

1112

1113 **Fig. 1.** (a) Tectonic map of the Piemont domain of the western Alps. (b). Geological
1114 map of the Chenaillet massif (star in Fig 1a, modified after Lafay et al., 2017)
1115 showing the location of the ophicarbonates outcrops and investigated samples.

1116 **Fig. 2.** SEM-BSE images of representative textures observed in the Chenaillet
1117 ophicarbonates. (a) Serpentine mesh textures with and without C2 calcite partially
1118 replacing serpentine in mesh cores (sample RL6). (b) Complex mesh textures
1119 showing inner and outer cores surrounded by magnetite; inner cores are locally fully
1120 replaced by C2 calcite (sample RL6). (c) Mesh inner and outer cores completely
1121 replaced by C2 calcite (sample RL6). (d) Hourglass serpentine associated with
1122 magnetite (sample RL9). (e, f) Lizardite+magnetite veinlets (V-1) following original
1123 grain boundaries (samples RL3 and RL10). (g) Large lizardite+magnetite vein (V-2)
1124 crosscutting mesh textures (sample RL6). (h) C1 calcite vein crosscutting V-2 veins
1125 (sample RL6). (i) Textural link between C2 calcite in mesh textures and C1 calcite
1126 veins (sample RL10). (j, k) Lizardite+dolomite layers within the C3 calcite matrix
1127 containing a relict spinel (Spl); C3 calcite matrix is associated with small chrysotile
1128 grains (Ctl) and sometimes crosscut by calcite veins free of serpentine (C3-vein)
1129 (sample RL6). (l) Chrysotile grains in C3 calcite matrix (sample RL6). White and red
1130 circles are oxygen ($\delta^{18}\text{O}_{\text{VSMOW}}$, ‰) and carbon ($\delta^{13}\text{C}_{\text{VPDB}}$, ‰, in parentheses) isotope
1131 SIMS pits, respectively. Srp = serpentine, Ctl = chrysotile, LZ = lizardite, Cal =
1132 calcite, Dol = dolomite, Mag = magnetite, Spl = Cr-spinel.

1133 **Fig. 3.** SEM-CL images showing representative CL features in (a-c) C1 calcite veins
1134 (samples RL9, RL3 and RL10) and (d-i) C2 calcite mesh (samples RL6, RL10 and
1135 RL9). C1 veins are sometimes rimmed by a distinct brighter (b) or darker (c) CL

1136 layer. C2 calcite mesh have marked euhedral (g, i) to anhedral (f, h) CL zonation.
1137 Resorption features are sometimes observed in C2 calcite mesh (f-i). White and red
1138 circles are locations of oxygen ($\delta^{18}\text{O}_{\text{VSMOW}}$, ‰) and carbon ($\delta^{13}\text{C}_{\text{VPDB}}$, ‰, in
1139 parentheses) isotope SIMS pits, respectively.

1140 **Fig. 4.** SEM-BSE images of representative dolomite textures in the Chenaillet
1141 ophicarbonates. Dolomite is observed as (a) rims around C2 calcite mesh (sample
1142 RL9), (b) borders along C1 calcite veins at the contact with serpentine (sample RL7),
1143 (c) subhedral grains in the lizardite layers at the boundary between serpentinite clasts
1144 and C3 calcite matrix (sample RL6), (d) borders between C4 calcite vein and
1145 serpentinite clast (sample RL9). White and red circles are oxygen ($\delta^{18}\text{O}_{\text{VSMOW}}$, ‰)
1146 and carbon ($\delta^{13}\text{C}_{\text{VPDB}}$, ‰, in parentheses) isotope SIMS pits, respectively.

1147 **Fig. 5.** SEM-CL images showing representative CL features in the carbonate matrix
1148 surrounding serpentinite clasts (samples RL6 and RL10). Domains with large calcite
1149 grains (C1') showing concentric (a-b) or oscillatory CL zoning (c) are surrounded by
1150 an aggregate of fine-grained calcite+chrysotile (a-b). (a, c) Large calcite grains in C1'
1151 domains are crosscut or bounded by calcite veinlets (C1'-veins). (d) Sharp contact
1152 between a calcite C3-vein and the surrounding fine-grained calcite matrix (C3). White
1153 and red circles in (c) and (d) are locations of oxygen ($\delta^{18}\text{O}_{\text{VSMOW}}$, ‰) and carbon
1154 ($\delta^{13}\text{C}_{\text{VPDB}}$, ‰, in parentheses) isotope SIMS pits, respectively. Dashed lines in (a) to
1155 (c) are locations of SIMS oxygen and carbon isotope traverses (see Electronic
1156 Appendix B).

1157 **Fig. 6.** Summary of oxygen isotope data in serpentine from the Chenaillet
1158 ophicarbonates measured by SIMS.

1159 **Fig. 7.** Summary of oxygen isotope data in carbonate from the Chenaillet
1160 ophicarbonates measured by SIMS.

1161 **Fig. 8.** Serpentine-magnetite thermometry. (a) Calculation of equilibrium
1162 temperatures for serpentine-magnetite pairs in different textures based on SIMS-
1163 measured mineral $\delta^{18}\text{O}$ values. (b) Calculation of water oxygen isotope values in
1164 equilibrium with both serpentine and magnetite in different textures based on
1165 calculated equilibrium temperatures. Solid and dashed lines are calculated equilibrium
1166 temperatures based on serpentine-water oxygen isotope fractionation factors by Fröh-
1167 Green et al. (1996) and Saccocia et al. (2009), respectively. Magnetite-water oxygen
1168 isotope fractionation factors are after Bottinga and Javoy (1973).

1169 **Fig. 9.** Serpentine-carbonate thermometry. (a) Calculation of equilibrium
1170 temperatures for lizardite+dolomite and chrysotile+calcite pairs based on SIMS-
1171 measured mineral $\delta^{18}\text{O}$ values. (b) Calculation of water oxygen isotope values in
1172 equilibrium with serpentine, dolomite and calcite in each pair based on calculated
1173 equilibrium temperatures. Solid and dashed lines are calculated equilibrium
1174 temperatures for dolomite-serpentine (Matthews and Katz, 1977; Fröh-Green et al.,
1175 1996) and calcite-serpentine (O'Neil et al., 1969; Fröh-Green et al., 1996),
1176 respectively.

1177 **Fig. 10.** Summary of the different mineral generations and corresponding $\delta^{18}\text{O}$ values
1178 (‰). Formation is attributed to four stages of hydrothermal alteration in the Chenaillet
1179 ophicarbonates.

1180 **Fig. 11.** Schematic illustration showing the progression of textural and T - $\delta^{18}\text{O}_{(\text{water})}$
1181 variations in the Chenaillet ophicarbonates. Ol = olivine, Opx = orthopyroxene, Cr-
1182 Spl = Cr-spinel, Srp_C = serpentine mesh core, Srp_R = serpentine mesh rim, Mag =
1183 magnetite, Lz = lizardite, Dol = dolomite, Ctl = chrysotile. $\delta^{18}\text{O}_W$ = oxygen isotope
1184 values of water.

1185 **Fig. 12.** Simplified cross section showing the evolution of the hydrothermal system
1186 presented in this study in a seafloor tectonic setting (modified after Manatschal et al.,
1187 2011 and Lafay et al., 2017). Numbers correspond to the stages of alteration shown in
1188 Fig. 11.

1189

1190 **Table 1.** Serpentine-magnetite thermometry for ophicarbonates from the Chenaillet
1191 ophiolite.

1192 **Table 2.** Serpentine-dolomite thermometry in hourglass textures for ophicarbonates
1193 from the Chenaillet ophiolite.

1194

1195 **SUPPLEMENT FIGURE AND TABLE CAPTIONS**

1196

1197 **Fig. A.1.** SEM-BSE maps of thin sections from the investigated samples from the
1198 Chenaillet ophiolite.

1199 **Fig. A.2.** Diagrams showing the major and minor element chemical composition of
1200 serpentine in different textural locations in the various investigated samples. Cal =
1201 calcite, Srp = serpentine.

1202 **Fig. A.3.** SEM-BSE images showing “turbid” calcite domains associated with
1203 chrysotile grains (C3) and “clear” calcite domains lacking chrysotile (C1’) in the
1204 carbonate matrix surrounding serpentinite clasts (Chenaillet ophicarbonates).

1205 **Fig. A.4.** (a) SIMS oxygen isotope edge-to-edge traverse across a large (~1 mm) C1
1206 calcite vein shown in Fig. 3c. SEM-CL (b) and SEM-BSE (c) images in a different
1207 area of the same vein showing ~ 3‰ variation in $\delta^{18}\text{O}$ values. White and red circles
1208 are locations of oxygen ($\delta^{18}\text{O}_{\text{VSMOW}}$, ‰) and carbon ($\delta^{13}\text{C}_{\text{VPDB}}$, ‰, in parentheses)
1209 isotope SIMS pits, respectively.

1210 **Fig. A.5.** Plot of $\delta^{18}\text{O}$ versus $\delta^{13}\text{C}$ in different calcite generations from the Chenaillet
1211 ophicarbonates.

1212 **Fig. A.6.** BSE-SEM images of SIMS pits on magnetite from the Chenaillet
1213 ophicarbonates. (a) Mesh texture (sample RL6), (b) V-1 vein (sample RL3), (c) V-2
1214 vein (sample RL6), and (d) hourglass texture (sample RL9). White areas are remnants
1215 of Au coating. White circles are locations of oxygen ($\delta^{18}\text{O}_{\text{VSMOW}}$, ‰) isotope SIMS
1216 pits.

1217 **Fig. A.7.** Model showing the net variation in oxygen isotope ratios in both serpentine
1218 and magnetite as a function of a contemporary variation in temperature and water
1219 $\delta^{18}\text{O}$. Serpentine-water and magnetite-water oxygen isotope fractionation factors are
1220 after Fröh-Green et al. (1996) and Bottinga and Javoy (1973), respectively.

1221 **Fig. A.8.** Representative SEM-BSE images of SIMS pits in serpentine (a), calcite (b),
1222 dolomite (c) and magnetite (d).

1223

1224 **Table A.1.** Complete data table for oxygen isotope analyses by SIMS (A.1a) and
1225 corresponding EPMA (A.1b) in serpentine from the Chenaillet ophicarbonates.

1226 **Table A.2.** Complete data table for oxygen (A.2a) and carbon (A.2b) isotope analyses
1227 by SIMS as well as representative EPMA (A.2c) in carbonate from the Chenaillet
1228 ophicarbonates.

1229 **Table A.3.** Complete data table for oxygen isotope analyses in magnetite by SIMS
1230 (A.3a) and representative EPMA (A.3b) from the Chenaillet ophicarbonates.

1231 **Table A.4.** Complete data table for oxygen (A.4a) and carbon (A.4b) isotope analyses
1232 by SIMS in carbonate and magnetite (A.4c) reference materials. Data on serpentine
1233 reference materials are published in Scicchitano et al. (2020) in supplementary Table
1234 S2 (sessions S6 and S8).

1235 **Table A.5.** Serpentine-magnetite thermometry for ophicarbonates from the Chenaillet
1236 ophiolite using different serpentine-magnetite calibrations.

1237 **Table 1.** Serpentine-magnetite thermometry for ophicarbonates from the Chenaillet ophiolite.

Analysis ID	Texture	$\delta^{18}\text{O}$ (‰)	$\delta^{18}\text{O}$ (‰)	$\Delta^{18}\text{O}$ (Srp-Mag)	T (°C)*	$\delta^{18}\text{O}_w$ (‰)*	T (°C)**	$\delta^{18}\text{O}_w$ (‰)**
		<i>serpentine</i>	<i>magnetite</i>		<i>calculated</i>	<i>calculated</i>	<i>calculated</i>	<i>calculated</i>
RL6-1-(Srp-18b/Mag-1)	mesh	6.6	-6.0	12.7	196	4.3	245	3.1
RL6-1-(Srp-18b/Mag-2)	mesh	6.6	-5.6	12.2	204	4.5	252	3.4
RL6-1-(Srp-20/Mag-3)	mesh	6.7	-5.7	12.5	199	4.5	248	3.4
RL6-1-(Srp-34/Mag-4)	mesh	6.6	-10.2	16.9	136	2.1	194	0.0
RL6-1-(Srp-24/Mag-5)	mesh	7.8	-6.3	14.2	172	4.7	225	3.2
RL6-1-(Srp-25/Mag-7)	mesh	7.4	-5.5	12.9	192	5.0	242	3.7
RL6-1-(Srp-27/Mag-8)	mesh	6.3	-9.8	16.3	144	2.2	201	0.3
RL6-1-(Srp-29/Mag-9)	mesh	6.8	-6.3	13.2	188	4.2	239	2.9
RL6-1-(Srp-41/Mag-17)	mesh	7.2	-5.1	12.3	202	5.1	250	3.9
RL6-1-(Srp-42/Mag-18)	mesh	7.4	-5.6	13.1	188	4.9	239	3.6
RL6-1-(Srp-50/Mag-19)	mesh	5.2	-9.6	15.0	161	1.8	216	0.1
RL6-1-(Srp-49/Mag-21)	mesh	6.9	-10.2	17.3	132	2.2	191	0.1
RL6-1-(Srp-49/Mag-22)	mesh	6.9	-9.5	16.5	141	2.6	198	0.6
RL6-2-(Srp-28/Mag-13)	mesh	7.4	-5.0	12.6	198	5.2	247	4.0
RL6-2-(Srp-27/Mag-14)	mesh	7.2	-7.6	14.9	162	3.7	217	2.1
RL6-2-(Srp-26/Mag-15)	mesh	7.5	-7.9	15.5	154	3.7	210	2.0
RL6-2-(Srp25/Mag-16)	mesh	7.4	-8.0	15.6	153	3.7	209	1.9
RL6-2-(Srp-13/Mag-5)	V-2 vein	4.1	-10.1	14.4	169	1.0	223	-0.6
RL6-2-(Srp-18/Mag-10)	V-2 vein	3.8	-7.7	11.6	215	2.0	261	1.1
RL3-(Srp-43/Mag-5)	V-1 vein	5.8	-8.2	14.1	173	2.8	226	1.3
RL9-(Srp-54/Mag-16)	hourglass Srp	5.2	-9.6	14.9	162	1.8	216	0.1
RL9-(Srp-58/Mag-18)	hourglass Srp	4.5	-8.4	13.1	190	2.0	240	0.7
RL9-(Srp-57/Mag-19)	hourglass Srp	4.6	-9.1	13.8	178	1.7	230	0.3
RL9-(Srp-56/Mag-20)	hourglass Srp	4.5	-8.0	12.5	198	2.3	247	1.1

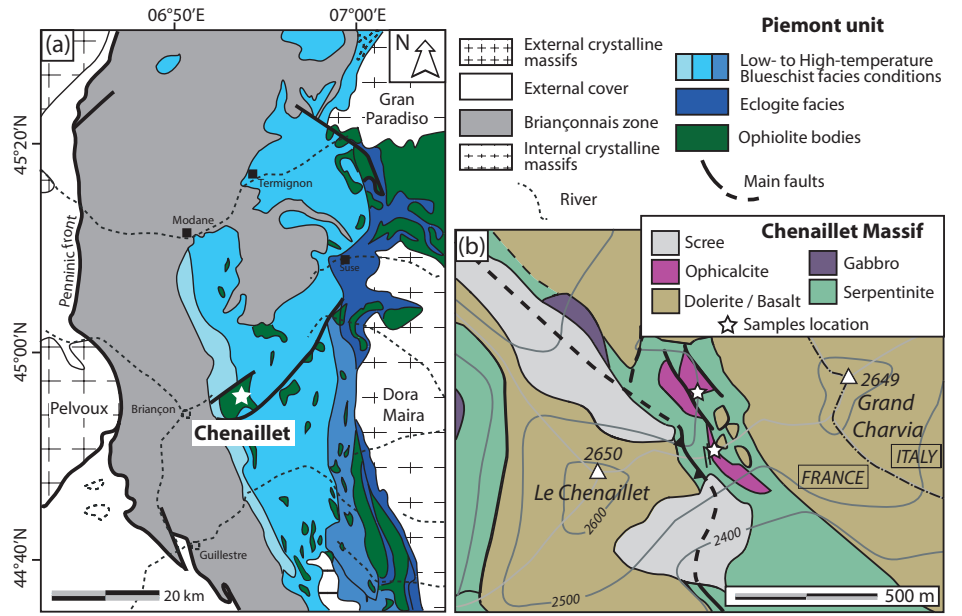
* Srp-water after Früh-Green et al. (1996), ** Srp-water after Saccocia et al. (2009). Mag-water are after Bottinga and Javoy (1973). $\delta^{18}\text{O}_w$ = calculated oxygen isotope value of water in equilibrium with serpentine and magnetite.

1240 **Table 2.** Serpentine-dolomite thermometry in hourglass textures for ophicarbonates from the Chenaillet ophiolite.

Analysis ID	Texture	$\delta^{18}\text{O}$ (‰)	$\delta^{18}\text{O}$ (‰)	$\Delta^{18}\text{O}(\text{Dol-Srp})$	T (°C)	$\delta^{18}\text{O}_w$ (‰)
		<i>serpentine</i>	<i>dolomite</i>			<i>calculated</i>
RL9-1-(Srp-1/Dol-1)	hourglass	4.3	11.8	7.5	228	2.9
RL9-1-(Srp-4/Dol-2)	hourglass	4.4	11.7	7.3	235	3.1
RL9-1-(Srp-6/Dol-4)	hourglass	4.1	12.6	8.5	190	1.6
RL9-1-(Srp-10/Dol-5)	hourglass	4.3	12.0	7.6	220	2.7
RL9-1-(Srp-26/Dol-6)	hourglass	4.8	12.6	7.8	215	3.0
RL9-1-(Srp-29/Dol-10)	hourglass	4.3	12.2	7.9	213	2.5
RL9-1-(Srp-46/Dol-14)	hourglass	4.3	10.1	5.8	315	4.5
RL9-1-(Srp-51/Dol-15)	hourglass	4.3	12.5	8.2	200	2.1
RL9-1-(Srp-59/Dol-19)	hourglass	4.2	11.2	7.0	250	3.2
RL7-(Srp-4/Dol-4)	hourglass	4.6	10.9	6.3	285	4.3
RL7-(Srp-10/Dol-2)	hourglass	5.6	11.8	6.2	290	5.4
RL7-(Srp-9/Dol-1)	hourglass	5.0	11.6	6.6	270	4.4

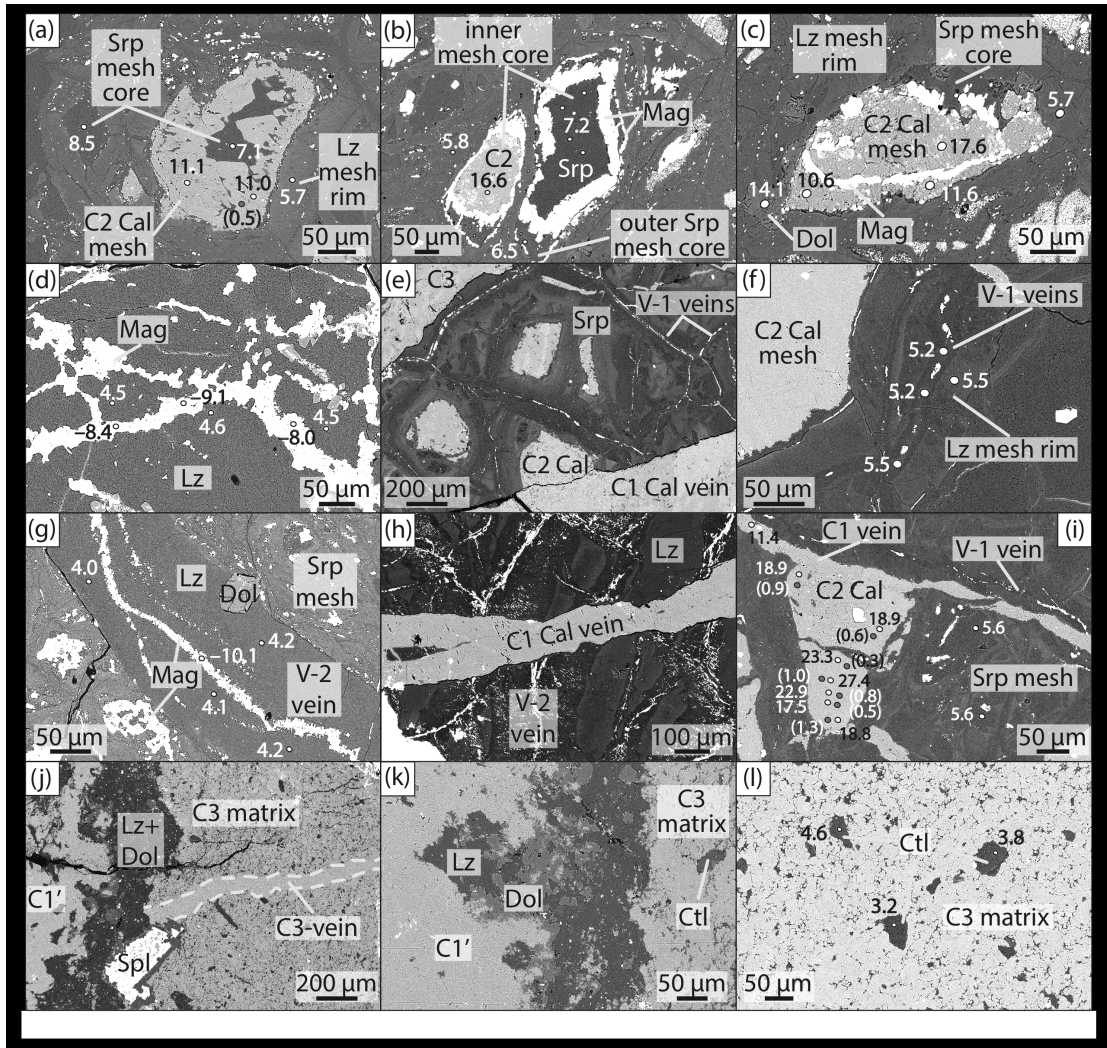
1241 Srp-water after Früh-Green et al. (1996), Dol-water after Matthews and Katz (1977). $\delta^{18}\text{O}_w$ = calculated oxygen isotope value of water in equilibrium with serpentine and
 1242 dolomite.

1243
 1244
 1245
 1246
 1247
 1248
 1249
 1250
 1251
 1252
 1253



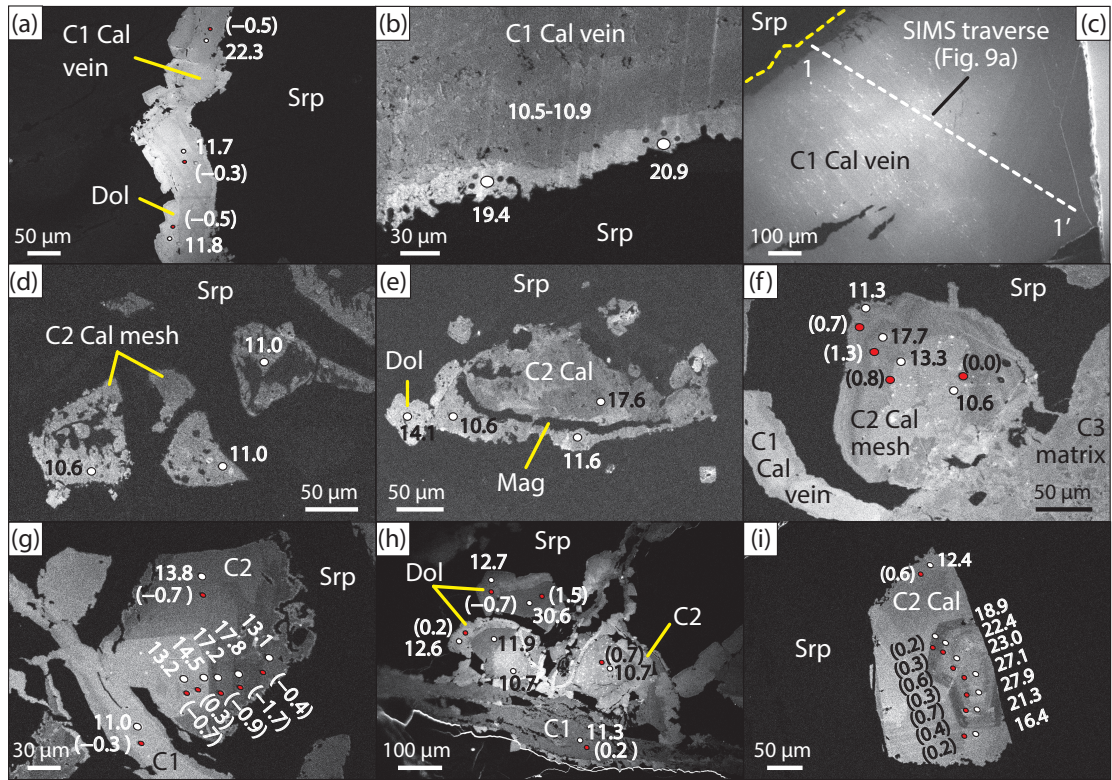
1254
1255

Figure 1



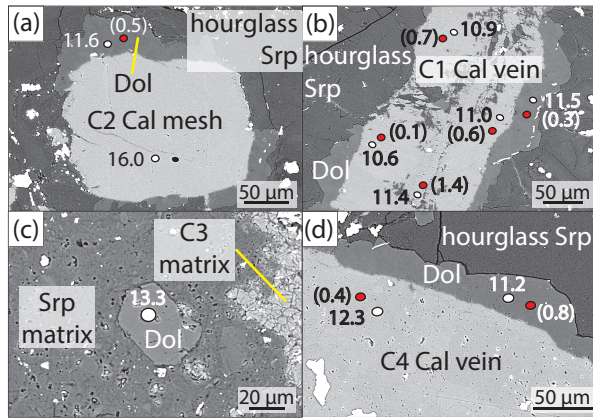
1256
 1257
 1258

Figure 2



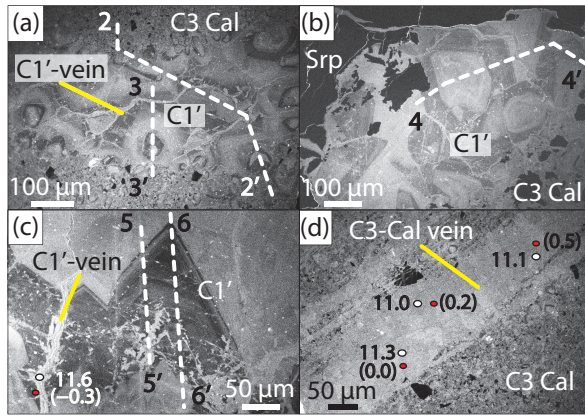
1259
1260

Figure 3



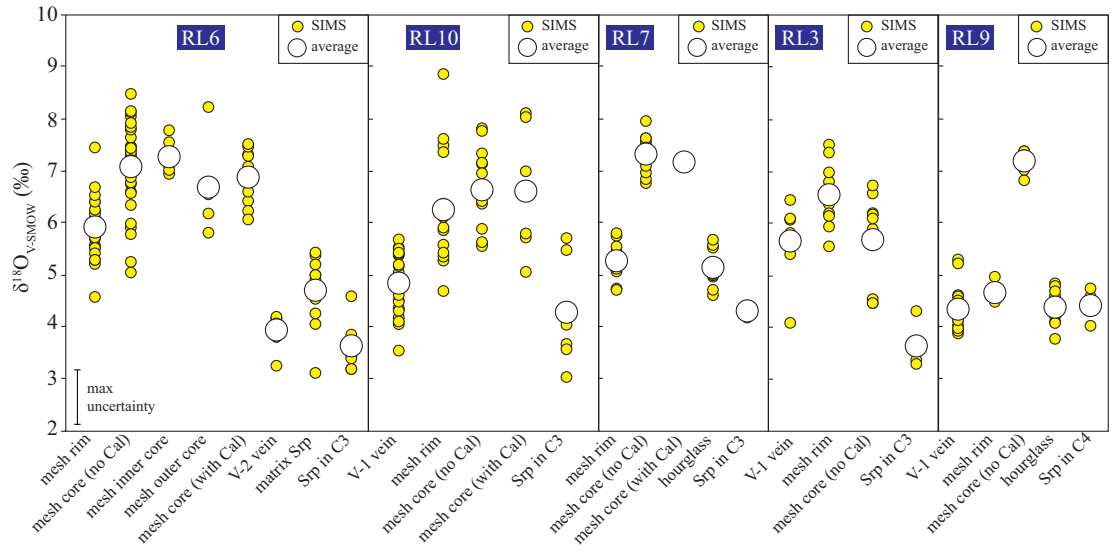
1261
1262

Figure 4



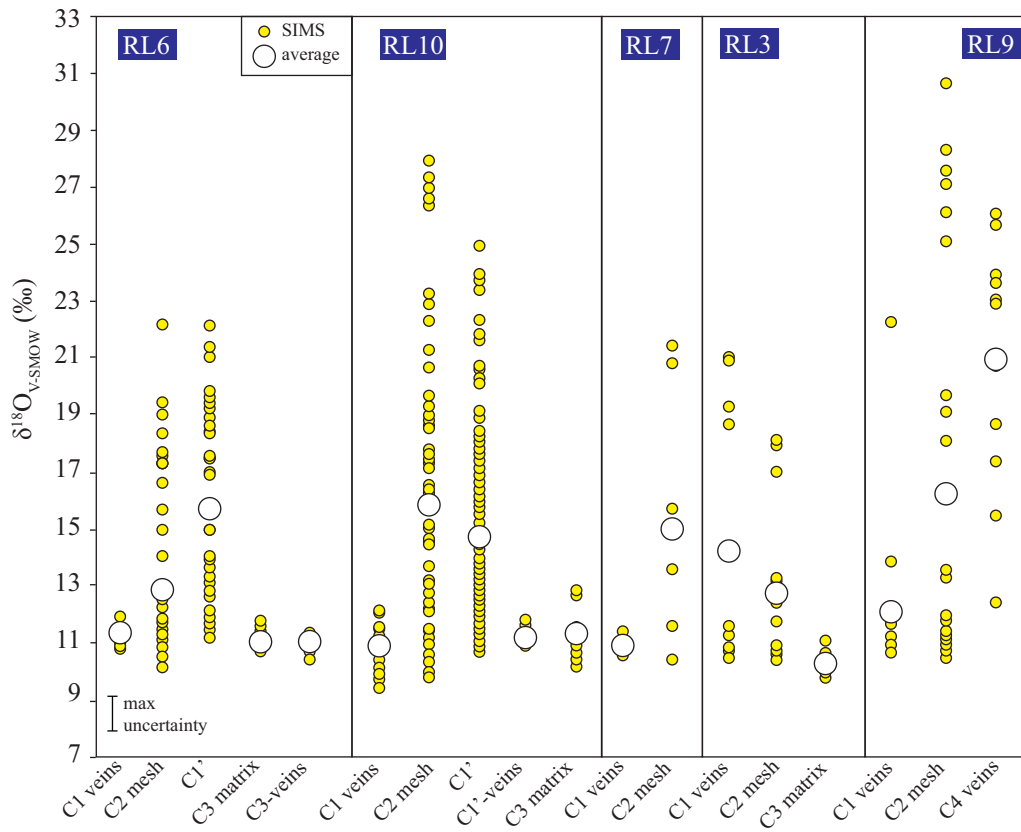
1263
1264

Figure 5



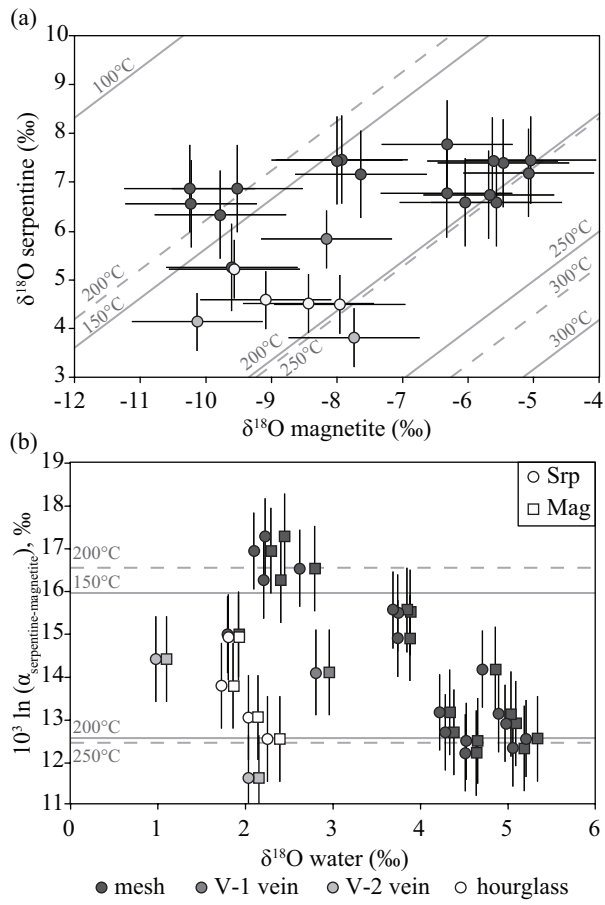
1265
1266

Figure 6



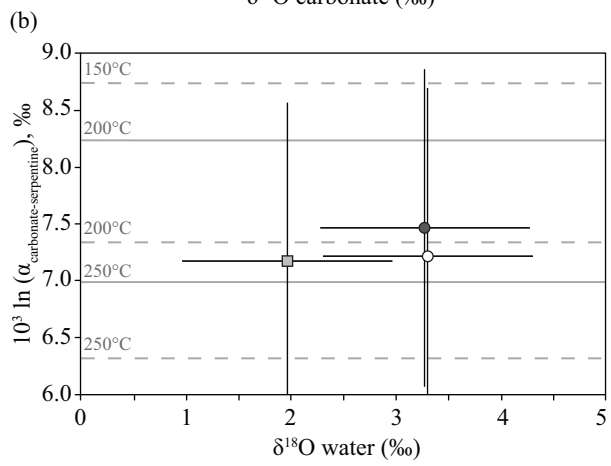
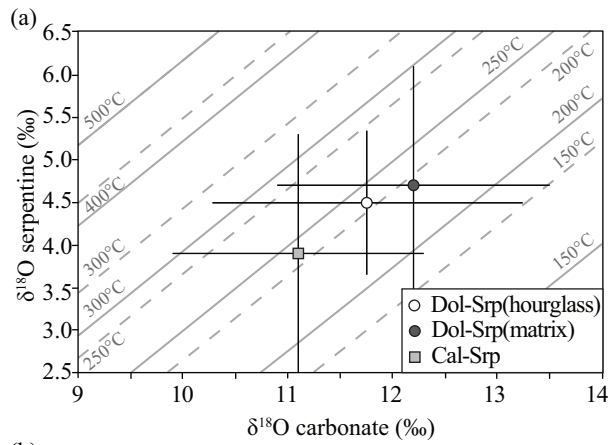
1267
1268

Figure 7



1269
1270

Figure 8



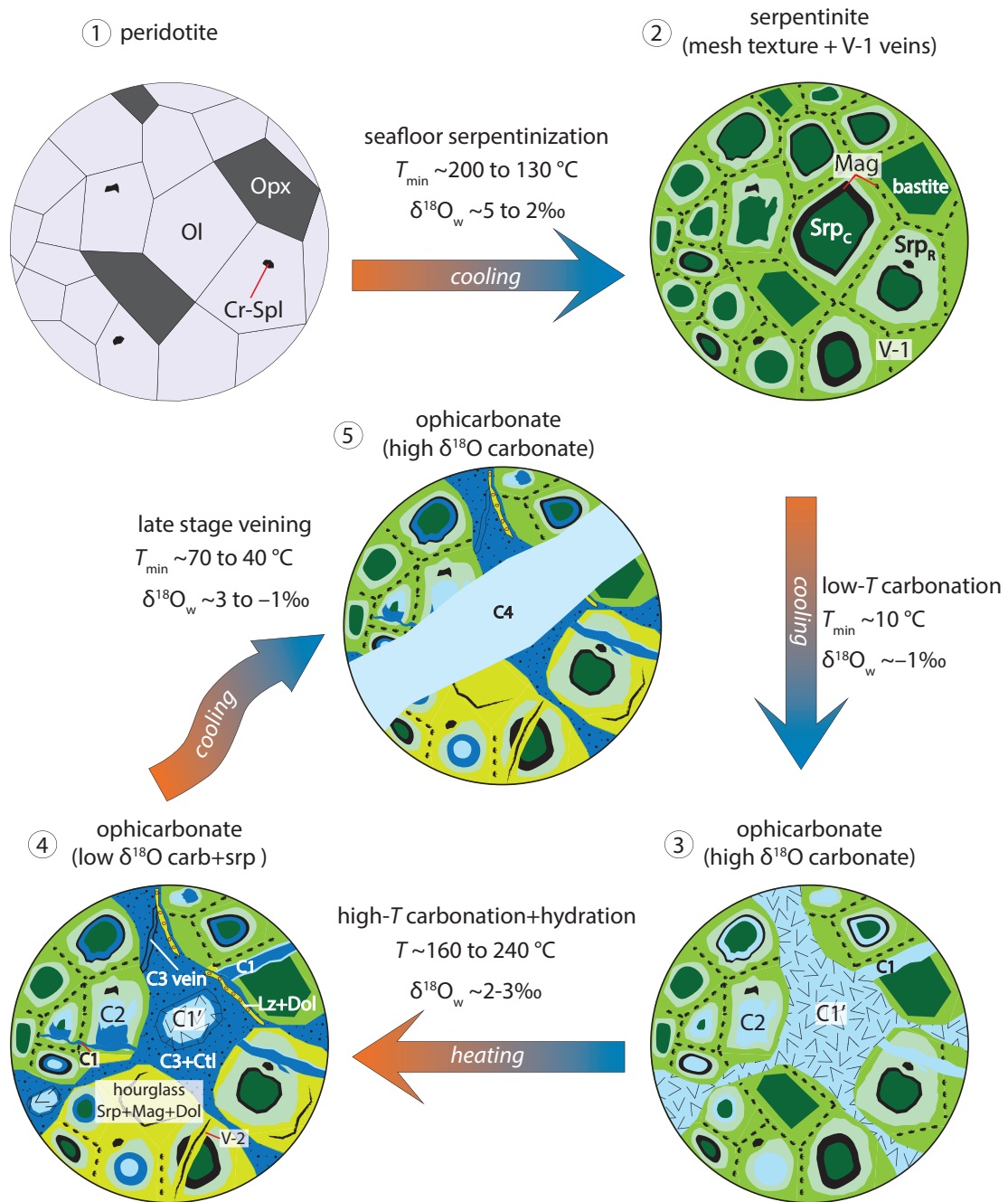
1271
1272

Figure 9

Stages Minerals	Early Serpentinization: $T_{\min} = 130-200\text{ }^{\circ}\text{C}$	Low-T Carbonation: $T_{\min} = 10\text{ }^{\circ}\text{C}$	High-T Serpentiniza- tion & Carbonation: $T = 160-240\text{ }^{\circ}\text{C}$	Late Carbonate Veining: $T_{\min} = 40-70\text{ }^{\circ}\text{C}$
Serpentine V-1 veins	3.5 to 6.4‰			
Serpentine mesh rims	4.5 to 8.8‰			
Serpentine mesh cores	4.4 to 8.5‰			
Magnetite V-1 veins	-8.5 to -7.3‰			
Magnetite mesh	-10.6 to -5.0‰			
Calcite C1 veins		22.3 to 9.4‰		
Calcite C2 mesh		30.6 to 9.8‰		
Calcite C1'		24.9 to 10.6‰		
Serpentine V-2 veins			3.2 to 4.2‰	
Serpentine hourglass			3.8 to 5.7‰	
Magnetite V-2 veins			-10.6 to -7.7‰	
Magnetite hourglass			-9.6 to -8.0‰	
Serpentine matrix			3.1 to 5.4‰	
Serpentine in C3 matrix			3.0 to 5.7‰	
Calcite C3 matrix			9.8 to 12.9‰	
Calcite C3-veins			10.5 to 11.5‰	
Calcite C1'-veins			10.9 to 11.8‰	
Dolomite		10.1 to 14.1‰	11.4 to 13.2‰	11.2 to 12.5‰
Calcite C4 vein				12.3 to 26.0‰
Serpentine in C4 vein				4.0 to 4.8‰

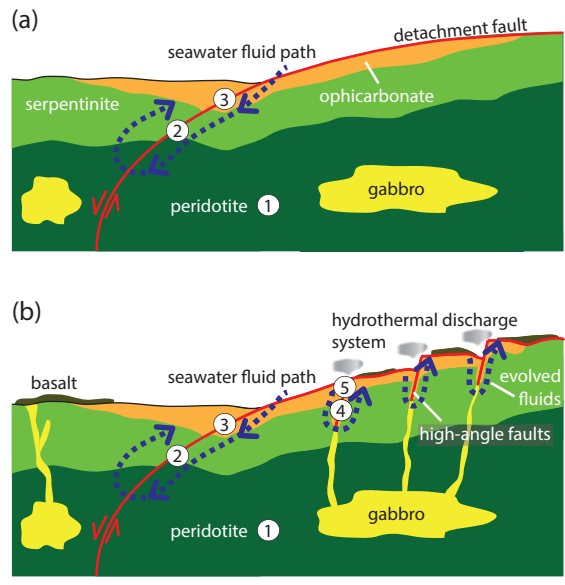
1273
1274

Figure 10



1275
1276

Figure 11



1277
1278

Figure 12